

MATHEMATICAL MODELING OF MICROSHRINKAGE
FORMATION DURING SOLIDIFICATION OF
A356 ALLOY CASTINGS

by

AKASH HIMANGSHU PATEL

LAURENTIU NASTAC, COMMITTEE CHAIR

NAGY EL-KADDAH
MARK WEAVER
BRIAN JORDAN

A THESIS

Submitted in partial fulfillment of the requirements for
the degree of Master of Science in the Department
of Metallurgical and Materials Engineering
in the Graduate School of
The University of Alabama

TUSCALOOSA, ALABAMA

2013

Copyright Akash Himangshu Patel 2013
ALL RIGHTS RESERVED

ABSTRACT

Significant efforts have been made by materials scientists and metallurgists to understand the underlying physics involved in solidification of aluminum alloys to predict a variety of casting defects. Shrinkage porosity is one of the most important types of casting defects. Addressing porosity has been a formidable challenge due to many contributing (and interacting) phenomena responsible for its formation and growth. Shrinkage porosity occurs by nucleation and growth phenomena. Very few previous models for shrinkage prediction consider the pore formation based on a nucleation and growth basis. Several models that can predict micro shrinkage in castings were revised in detail.

The main purpose of this study was to develop a comprehensive model which can predict micro-shrinkage pores that are forming during solidification of A356 castings. The model utilizes a stochastic approach and takes into consideration the Niyama criterion as well as the nucleation potential for formation of pores. Therefore, it can predict the random nature of pore formation during casting solidification. Correlations between the predictions and the pore amount were developed. For this model, literature validation was provided for an A356 alloy plate casting. Further validation was performed for a bar geometry cast in a silica sand mold. The model predictions match reasonably well with the experimental pore distribution profile.

LIST OF ABBREVIATIONS AND SYMBOLS

SDAS	Secondary Dendrite Arm Spacing
P	Metal pressure
η	Dynamic viscosity of liquid
\vec{g}	Gravity vector
ρ_{liq}	Density of liquid melt
K_{mz}	Permeability of mushy zone
P_{st}	Metallostatic pressure
P_{shr}	Negative pressure due to resistance to shrinkage induced flow through fixed dendrite skeleton
β	Shrinkage ratio
r_{feed}	Radius of the cylindrical feeding channel
L	Length of the mushy zone
ζ	Thermal function
ξ	Tortuosity factor
k_m	Thermal conductivity of mold
ρ_m	Density of mold
c_m	Specific heat of mold
ρ	Density of melt
ΔH	Latent heat of fusion
T_f	Liquidus temperature

T_o	Room temperature
V/A	Casting modulus
G_T	Thermal gradient
f_s	Fraction solid
Ny	Niyama criterion
Ny_{cr}	Threshold Niyama criterion
θ	Geometric parameter for feeding
ΔT_{SL}	Solidification interval
k_S	Thermal conductivity of solid
t_C	Solidification time for center of plate
l	Half the thickness of plate
Ny^*	Dimensionless Niyama criterion
G	Thermal gradient
λ_2	Secondary dendrite arm spacing
ΔP_{cr}	Critical pressure drop for stable pore to exist
\dot{T}	Cooling rate
ΔT_f	Freezing range
μ_l	Dynamic viscosity of liquid
θ	Dimensionless number
g_l	Liquid volume fraction
g_p	Final pore volume fraction
P_e	Local pressure in melt

V	Volume of bubble
A	Area of liquid-gas interface
γ	Interfacial energy per unit area
P_i	Pressure from the interior of bubble
ΔP^*	Critical pressure difference to form a pore
We	Weber number
Fr	Froude number
N_{ox}	Number of entrapped oxides resulted from the collision
α_1, α_2	Parameters depending on alloy composition
S	Collision surface area
u_{js1}, u_{js2}	Velocity of the free surfaces
S_{av}	Average surface area of the broken oxides
S_M	Surface area of the broken oxide film
l_v	Distance of oxide movement
Π_{ij}	Tensor of pulse flow velocity
ν	Kinematic viscosity
n	Normal vector to the solid surface
$S(r, t)$	Volume fraction of solid phase
$L(r, t)$	Volume fraction of liquid phase
$P(r, t)$	Volume fraction of empty phase
$\rho_s(T)$	Temporal evolution of density of solid phase
$\rho_L(T)$	Temporal evolution of density of liquid phases
$C_S^i(T)$	Concentrations of the i^{th} alloy component in solid phases

$C_L^i(T)$	Concentrations of the i^{th} alloy component in liquid phases
$Cp_S(T)$	Specific heat of solids as a function of time
$Cp_L(T)$	Specific heat of liquid as a function of time
$\lambda(T)$	Heat conduction coefficient with respect to time
q	Crystallization heat of alloy
P_n	Nucleation probability
N	Total amount of oxides
n	Local amount of oxides

ACKNOWLEDGEMENTS

It is my privilege being related to Professor Laurentiu Nastac, the only person without which this thesis would not have been possible. He has helped me walk my first steps in Metallurgical Engineering, made me understand the different perspectives related to the subject, improved my vision and provided guidance for my research. I appreciate all his efforts behind me and am grateful to him for being my guru in the truest sense.

I would like to acknowledge my friend Mohammad Farooq for helping me out in writing the code for the proposed model.

I would like to express my gratitude to Robert Fanning and my colleagues and friends, Xiaoda Liu and Shian Jia for their continuous support and for being with me during almost every experiment I performed.

I would like to thank my father who in spite of having finance background could understand what I was trying to do and also for being the person with whom I could discuss apart from my advisor. His criticism at every stage of my research had forced me to think beyond ideas available in literature.

Finally, I would also like to thank my mother, brother and my little sister for their never-ending love and support.

CONTENTS

ABSTRACT.....	ii
LIST OF ABBREVIATIONS AND SYMBOLS	iii
ACKNOWLEDGEMENTS.....	vii
LIST OF TABLES.....	x
LIST OF FIGURES	xi
1.0 INTRODUCTION	1
1.1 Motivation.....	2
1.2 Main Objectives	3
2.0 LITERATURE REVIEW	5
2.1 Porosity Types	5
2.2 General Shrinkage Behavior.....	5
2.3 Feeding Mechanisms for Shrinkage Porosity.....	8
2.4 Review of Criterion Functions.....	10
2.5 Dimensionless Numbers	25
2.6 Review on Modeling of Oxide Films.....	27
3.0 DESCRIPTION OF NUMERICAL MODEL	29
3.1 Novaflow Model [76]	29
3.2 Novasolid Model [76].....	30
3.3 Pore Nucleation Model	32
4.0 RESULTS AND DISCUSSION	35

4.1 Simulation Results	35
4.2 Experimental Results	42
5.0 CONCLUDING REMARKS AND FUTURE WORK	48
REFERENCES	50

LIST OF TABLES

Table I: Solidification shrinkage for some metals [5]	7
Table II: Fracture Pressure for liquids [5].....	20
Table III: Simulation Parameters	40

LIST OF FIGURES

Figure 1: Three types of shrinkage regimes: (a) Liquid contraction (b) Solidification Contraction (c) Solid contraction [5].	7
Figure 2: Five feeding mechanisms in a solidifying casting [5].	8
Figure 3: Pore location based on thermal gradient and plate thickness (T) [26].	12
Figure 4: Schematic illustration of geometric model by Sigworth and Wang [45].	14
Figure 5: Schematic diagram of mushy zone solidifying with constant temperature gradient, G and isotherm velocity, R [42].	16
Figure 6: Ellingham Diagram referring to the tendency of aluminum to oxidize [68].	21
Figure 7: (a) Effect of 1% of alloying element on aluminum at 800 °C (b) Growth of pure aluminum in a flow of oxygen, dry and moist air [5, 50].	23
Figure 8: Formation of bifilm AB and bubbles CD creating bubble trails [5].	24
Figure 9: Smoke simulation showing the increase in amount of surface turbulence [55].	25
Figure 10: Computer simulation of excess free surface of melt as a function of gate velocity [1].	26
Figure 11: Geometry of a pore in contact with a solid surface.	32
Figure 12: Flowchart for Matlab code	34
Figure 13: Modulus profile of for the 12.5 mm thickness cast A 356mm plate.	35
Figure 14: Solidification time profile for the 12.5 mm thickness cast A356 plate.	36
Figure 15: Profile for Niyama values for the cast A356 plate at 3% solid fraction.	36
Figure 16: Niyama plot shown from the top view of the A356 plate at 3% solid fraction.	37
Figure 17: Shrinkage contraction plot in the cast the A356 plate.	37
Figure 18: Distribution of oxides in the cast A356 plate.	38

Figure 19: Measurement location for shrinkage prediction [30].	38
Figure 20: Niyama versus wt. % pore based on the measurements shown in Fig. 18 [30].	39
Figure 21: Computer tomography (CT) scan showing volume of gas/shrinkage defects/mm ³ [30].....	39
Figure 22: Stochastic behavior of pore nucleation obtained through MATLAB code.....	40
Figure 23: Solidification time plot in the 20 mm×20 mm A356 bar geometry.	41
Figure 24: Niyama plot in the 20 mm×20 mm A356 bar geometry at 3% solid fraction.	41
Figure 25: Distribution of oxides in a cast bar geometry after solidification.	42
Figure 26: Stochastic behavior of pore nucleation obtained through MATLAB Code.....	42
Figure 27: Areal pore % observed at different metallographic cross-sections of the bar.....	44
Figure 28: Effect of Niyama criterion on pore percentage.	44
Figure 29: Comparing pore size with SDAS at an interval of 10 mm along the centerline of bar	45
Figure 30: Typical examples of micro-shrinkage observed on metallographic cross-sections at: (a) 210 mm, (b) 230 mm, (c) 170 mm (d) 150 mm and (e) 140 mm from end of the plate.	47

1.0 INTRODUCTION

Porosity is one of the most important types of casting defect. Addressing porosity has been a formidable challenge due to many contributing (and interacting) phenomena responsible for its formation and growth. There are many types of porosity [1], but the most severe is microporosity. Micro-pores act as local stress concentrators and crack initiation sites thereby negating the mechanical properties, especially on ductility and fatigue life. There are two main causes for formation of microporosity in castings: (a) shrinkage porosity due to volume change upon solidification combined with restricted flow during mushy zone region. (b) gas porosity caused by dissolved gases which condense upon solidification due to solubility difference of such in gases in liquid and solid media [2].

Significant effort has been made by materials scientists and metallurgists to understand the underlying physics involved in solidification of aluminum alloys to predict a variety of casting defects. These phenomena include restricted fluid flow in the solidifying metal, pore nucleation, soluble gas partitioning between the liquid and solid including its diffusion to pores and interaction of the pores with developing microstructure [3]. The objective of this thesis is to review the relevant literature models and develop a numerical model to predict shrinkage porosities and test the same on plate and bar geometries of A356 castings.

The cooling of metal from its pouring to solidification temperature is accompanied by density changes that induce motion of liquid metal in the volume of the casting. Stokes equation can be used for calculating metal pressure before dendrite coherency point. Beyond this point,

Darcy Law of flow through porous media can be applied. Their equations are as follows, respectively:

$$\nabla P = \eta \cdot \nabla^2 \vec{v} + \rho_{liq} \cdot \vec{g} \quad [1]$$

$$\nabla P = -\frac{\eta}{K_{mz}} \cdot \vec{v} + \rho_{liq} \cdot \vec{g} \quad [2]$$

Catalina et al. recently developed a simple model for calculating liquid metal pressure based on only density changes during solidification without the need to find the superficial velocity vector \vec{v} [4]. Their model does not account for the heterogeneous nucleation and growth kinetics of the shrinkage pores as well as pressure change due to the formation of gas pores.

1.1 Motivation

Porosity occurs by nucleation and growth phenomena. Very few previous models for shrinkage prediction consider the pore formation based on nucleation and growth basis. If the metal is exceptionally clean, i.e. without inclusions it is very difficult to nucleate a pore by homogenous nucleation. Strength of liquid metals is almost as high as that of solid metals with liquid metals being close-packed random structures whereas solid metals being regular close-packed structures. Non-metallic inclusions are potentially the weakest part of liquid metal (refer to Table II). Therefore, heterogeneous pore nucleation is more active in presence of non-metallic

inclusions like compounds of oxygen, sulphur, phosphorous or other nuclei which do not wet very well with the melt [5].

Presence of inclusions like oxides greatly increases the propensity of porosity formation in aluminum castings [6-10]. Along with thermal conditions, negative pressure for shrinkage pore formation there also exists a need of oxide nuclei (or other non-wetting inclusion) to create a pore. In my previous work on steel castings, there were often pores randomly generated in regions less susceptible to pore formation possibly due to oxide. So, our intention was to track the oxides generated and transported through fluid flow, trace them at the end of solidification and couple this information with the already well accepted Niyama criterion. In the later part of my research work, fundamental research on oxide formation, entrainment and growth appeared to me as equally important if not less than that to study pore formation. Not all non-metallic inclusions promote pore formation. Inclusions like borides, carbides and nitrides, which wet very well with melt act as grain refiners instead of nucleation site for pore formation. Wetting becomes very important to study because of the fact that nano-sized aluminum oxide (Al_2O_3) particles are used to obtain grain refinement and reduction of porosity in Aluminum Metal Matrix Nano Composite (MMNC) [11, 12, 13].

1.2 Main Objectives

The main objectives of this fundamental research are as follows:

- (1) To review the already existing criterion for predicting shrinkage.
- (2) To modify the Niyama criterion for pore prediction and develop a stochastic model to predict the randomized shrinkage pore formation in an A356 alloy based on the principles of heterogeneous nucleation.

(3) To validate this model for casting geometries (bars and plates) produced through the gravity-sand (silica sand) casting process.

The thesis is presented in the following sequence: chapter II provides a literature review, chapter III will present the model description, chapter IV will present and discuss in detail the modeling results and chapter V will present the conclusions and recommended future work.

2.0 LITERATURE REVIEW

2.1 Porosity Types

The porosity types can be defined based on the following:

Size:

- Macro-shrinkage: Such porosity is visible to the naked eye (bigger than 1 mm).
- Micro-shrinkage: Such porosity ranges on the scale of microns to less than 1 mm.

Cause:

- Shrinkage: Resulting from density difference between solid and liquid phases
- Gas: hydrogen is the major contributor of gas shrinkage in aluminum castings [14]
 - Due to solubility difference in solubility of gas in liquid and solid phase
 - Precipitated from solution of bifilms during solidification
 - Entrainment due to surface turbulence
 - Mechanically blown into the melt (eg. Core blow) [14]

2.2 General Shrinkage Behavior

Molten metal occupies considerably more volume than the solidified castings. Metal contracts at three different rates when cooling from its liquid state (addition of liquidus temperature and the amount of superheat) to room temperature [14].

- (a) Liquid Contraction: As temperature reduces, first contraction is observed in liquid state. Such contraction is not troublesome because the extra liquid metal required to

compensate for this small reduction in volume is provided without difficulty resulting in a slight fall in level in the feeder.

(b) Solidification Contraction: This contraction is a result of density difference between melt at solidus and liquidus temperature. Solidification shrinkage for some metals is shown in Table I. This contraction causes several issues including:

- Requirement for 'feeding' which allows for compensation of contraction during solidification.
- 'Shrinkage porosity' resulting from improper feeding mechanism.

(c) Solid Contraction: Cooling from solidus temperature to room temperature results into metal contraction. Problems associated with such contraction includes:

- Patternmakers allowance or contraction allowance needs to be considered into casting design which is difficult to quantify.
- Mold constraint during solid contraction may lead to localized defects like hot tearing or cracking.

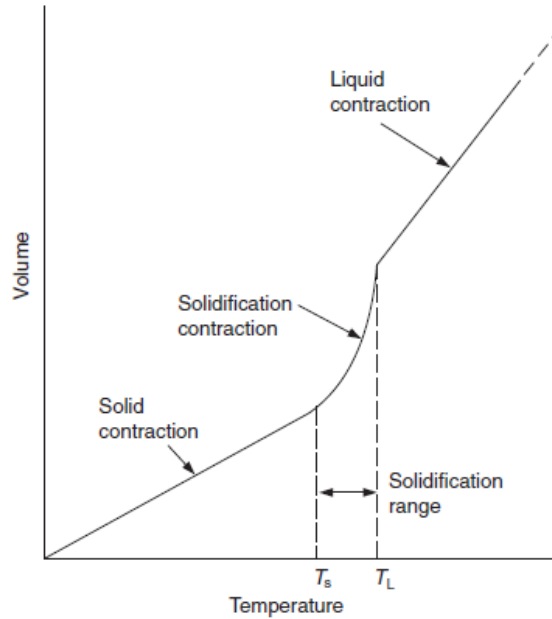


Figure 1: Three types of shrinkage regimes: (a) Liquid contraction (b) Solidification Contraction (c) Solid contraction [5].

Table I: Solidification shrinkage for some metals [5]

Metal	Crystal structure	Melting point °C	Liquid density (kgm ⁻³)	Solid density (kgm ⁻³)	Volume change (%)	Ref.
Al	fcc	660	2368	2550	7.14	1
Au	fcc	1063	17 380	18 280	5.47	1
Co	fcc	1495	7750	8180	5.26	1
Cu	fcc	1083	7938	8382	5.30	1
Ni	fcc	1453	7790	8210	5.11	1
Pb	fcc	327	10 665	11 020	3.22	1
Fe	bcc	1536	7035	7265	3.16	1
Li	bce	181	528	-	2.74	4, 5
Na	bcc	97	927	-	2.6	4, 5
K	bcc	64	827	-	2.54	4, 5
Rb	bce	303	11 200	-	2.2	2
Cd	bep	321	7998	-	4.00	2
Mg	bep	651	1590	1655	4.10	3
Zn	sep	420	6577	-	4.08	2
Ce	bep	787	6668	6646	-0.33	1
In	tel	156	7017	-	1.98	2
Sn	tetrag	232	6986	7166	2.51	1
Bi	rbomb	271	10 034	9701	-3.32	1
Sb	rhomb	631	6493	6535	0.64	1
Si	diam	1410	2525	-	-2.9	2

2.3 Feeding Mechanisms for Shrinkage Porosity

As freezing liquid contracts to form solid, internal pressure may fall far enough to become negative. Such negative pressure differentials provide the driving force for initiation and growth of volume defects such as porosity and surface sinks on castings. There are five feeding mechanisms leading to reduction in hydrostatic tension [15]. A more recent study by Dahle et al. confirms this hypothesis [16, 17].

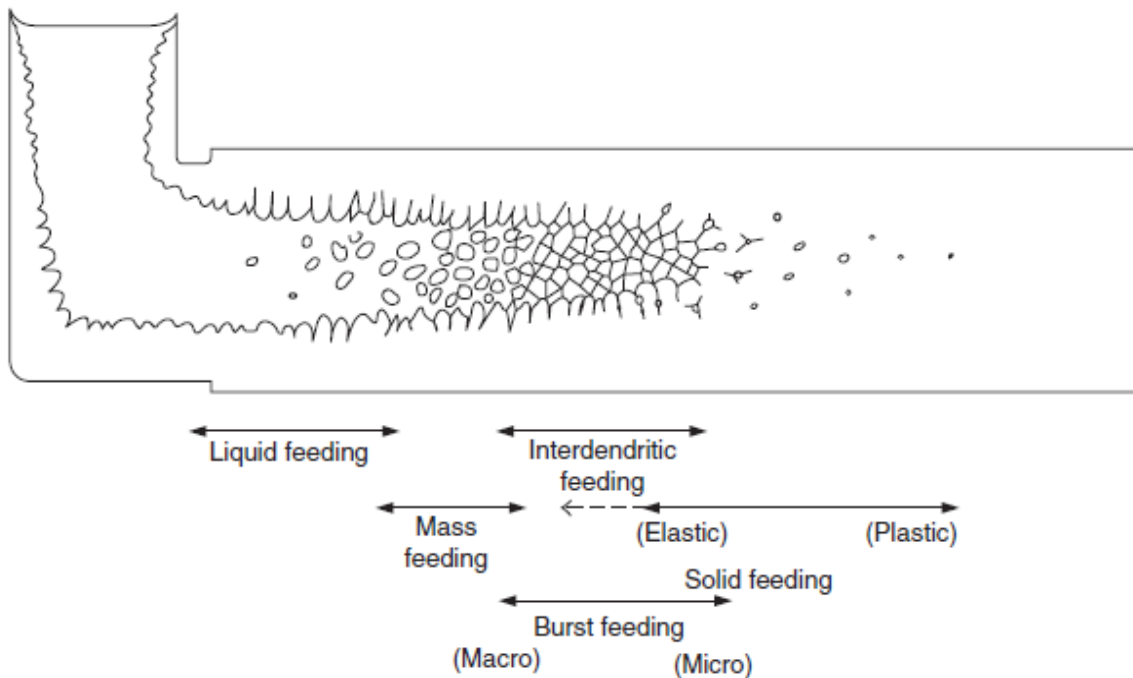


Figure 2: Five feeding mechanisms in a solidifying casting [5].

Liquid Feeding: Since liquid metal has low viscosity (near to that of water) this mechanism works effectively at negligibly small pressure gradients. Skin-forming alloys such as pure metals and eutectics will have a smooth solidification front resulting in a smooth shrinkage pipe and this

mechanism is the only form of feeding mechanism. Long freezing range alloys will solidify solidified in the form of a mesh of dendrites and hence interdendritic feeding becomes more crucial compared to liquid feeding.

Mass Feeding: Feeding occurs by such mechanism when volume fraction of solid reaches between 0 and 50%, depending on the pressure differential driving the flow and percentage of dendrites free from points of attachments to the casting wall.

Interdendritic Feeding: As metal solidifies, dendrite mesh thickens causing the interdendritic channels to become narrower and progressively restrain of residual liquid. Such mechanism is crucial for long freezing range alloys. Piwonka et al. utilized Darcy's law for the flow of residual liquid through coherent network of dendrites [18, 19].

$$P_{st} - P_{shr} = \frac{32\mu\beta\zeta^2 L^2 \xi^2 \lambda_l^2}{(1-\beta)r^4 \pi r_{feed}^4} \quad [3]$$

where β is shrinkage ratio, r_{feed} is the radius of the cylindrical feeding channel, L is the length of the mushy zone, r is the radius of feeding capillary and ζ is a thermal function and ξ is the tortuosity factor.

Burst Feeding: Feeding that may occur due to sudden yield of feeding barrier such that feed metal suddenly bursts in poorly fed region is known as burst feeding. It is of lesser significance and such mechanism is not supported by much proof.

Solid Feeding: It describes the condition when a region of casting has been isolated from feed liquid supply. As the residual liquid freezes it progressively occupies lesser space. There are two options to account for this space. One alternative is to grow as a shrinkage or gas pore and the other option is for the solid shell of casting to collapse inwards under internal reduced pressure, making up for the volume deficit. Solid feeding therefore relieves hydrostatic tensile stress built up by inward flow of the solid. If yield stress of solid shell is low as in aluminum alloys, then solid feeding is much dominant compared to steels.

2.4 Review of Criterion Functions

The mathematical complexity of the numerical models for shrinkage porosity prediction and lack of reliable and repeatable experimental database [20] have led a number of researchers to develop simpler analytical equations termed as “Criterion Functions” to predict regions of the casting with maximum probability of defects. Criterion functions are simple empirical rules that relate local conditions (e.g., cooling rate, thermal gradient, solidification velocity, etc.) in order to predict defects [19]. Berry, Spittle and their respective coworkers have reviewed certain of the existing criteria proposed [21, 22].

Chvorinov’s Criterion: Chvorinov (1940) proposed a famous feeding criterion function to avoid shrinkage in casting. According to this criterion, the feeder must solidify after the casting.

Solidification time was based modulus (total volume / total cooling surface area) of the casting based on 1-D heat transport across mold-metal interface [23].

$$t_f = \frac{\pi}{4} \left(\frac{1}{k_m \rho_m c_m} \right) \left(\frac{\rho \nabla H}{T_f - T_o} \right)^2 \left(\frac{V}{A} \right)^2 \quad [4]$$

where t_f is solidification time, k_m is thermal conductivity of mold, ρ_m is density of mold, c_m is specific heat of mold, ρ is density of melt, ΔH is latent heat of fusion, T_f is liquidus temperature, T_o is room temperature and V/A is modulus of the casting.

Limitations: This modulus based criterion may only be used as a rough approximation as it does not consider the shape factor (good thing is its size independent) and orientation of casting compared to the feeder.

Pellini Criterion: Pellini (1953) formulated a criterion which states that a shrinkage defect may occur in a region where the thermal gradient is smaller than a critical value, $G_T < G_T^{cr}$, at the end of solidification (when $f_s = 1$ or $f_s < f_s^{cr}$). Based on experimentation on carbon steels in green sand molds he related feeding distance (L) to section thickness of plates (T). He concluded that plates castings are free from pores along the length of (provided that alloy is well degassed) $2.5T$ due to chilling effect of casting edge and remaining $2.0T$ due to the feeder [24, 25].

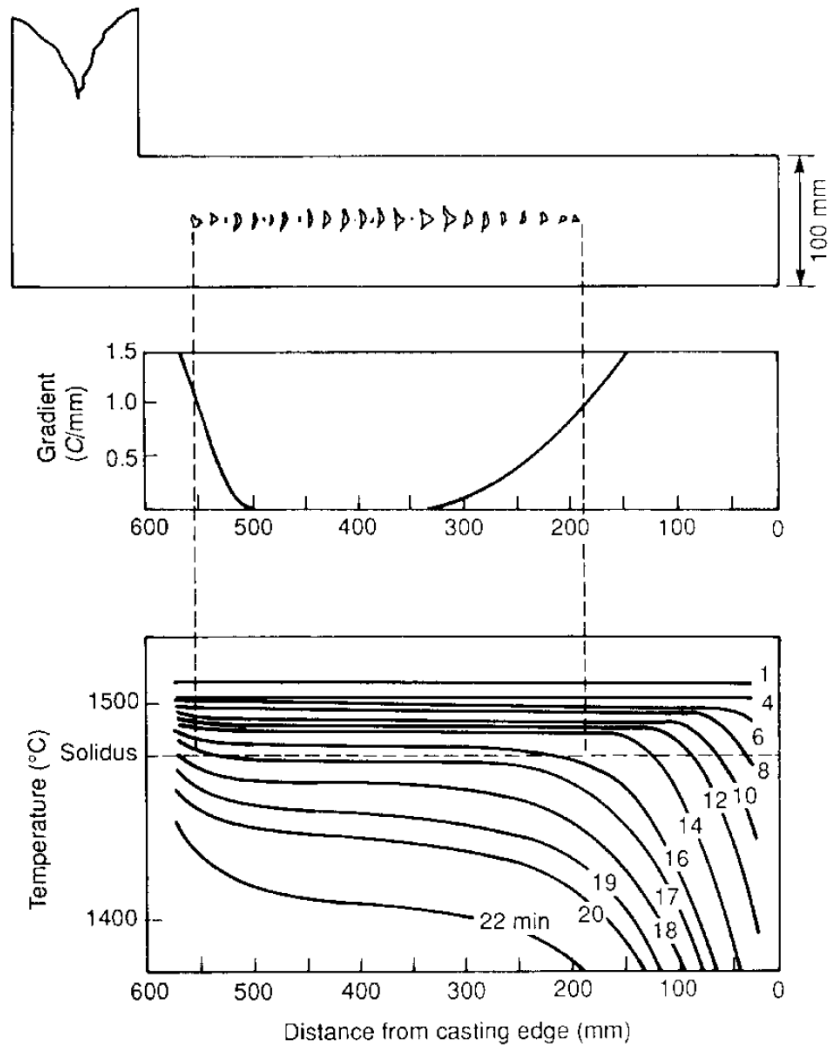


Figure 3: Pore location based on thermal gradient and plate thickness (T) [26].

Limitations:

- Hansen and Sahn (1988) pointed out that the critical thermal gradient to avoid shrinkage porosity in a steel bar is five to ten times more than that required for a plate geometry. Critical thermal gradient in a cylindrical steel casting depends on its diameter. Hence, this criterion cannot work for all geometries [27].

- Kubo and Pehlke (1985) developed a theoretical model which was in agreement with Pellini's results for steel castings, but not for Al-4.5Cu alloy [28]. Therefore, it changes for different alloy systems and so more sophisticated models were necessary to predict shrinkage.

Niyama Criterion: Niyama et al. (1982) elaborated on Pellini's idea developing a new criterion for low-carbon steel castings. They used Darcy's law in cylindrical coordinates to relate fluid velocity to pressure drop in the mushy zone, Carman-Kozeny model to calculate permeability of the mushy zone, assumed no gas fraction g_p (no gas pore) and expressed pressure drop in the mushy zone as an inverse of $\frac{G_t^2}{dT/dt}$.

Niyama value is computed as follows:

$$Ny = \frac{G_t}{\sqrt{dT/dt}}; Ny < Ny_{cr} \quad [5]$$

where G_t is the thermal gradient and dT/dt is the cooling rate. Based on his experiments, Niyama stated that the shrinkage defects are more susceptible to occur in casting locations where Ny is less than some critical Niyama value (Ny_{cr}) which is alloy dependent [29]. Critical Niyama value (or threshold Niyama value) for steels is $1 \text{ K}^{1/2} \text{ s}^{1/2} \text{ mm}^{-1}$. There is much experimental validation of Niyama criterion to prove its validity and applicability [29 – 35].

Advantages:

- Cooling rate and gradient are easy to determine in the casting. Hence this criterion can be applied with ease
- Experimentally proven for steel alloys

Limitations:

- Threshold Niyama value ($N_{y,cr}$) is alloy dependent. Experimental validation of this threshold value is required before using it for alloy systems other than steels
- Does not provide pore size and pore distribution
- It does not lend any insight into the nucleation and growth of pores

Geometric Model by Sigworth and Wang: Sigworth and Wang proposed a “geometric” model of the solidification process as shown in Figure 1 which represents schematically the cross section of a solidifying plate casting. The dark area in the center of the plate represents the tapered liquid pool. They determined the critical thermal gradient as a function of the angle of inner feeding channel inside the casting, θ required to avoid micro-shrinkage [36].

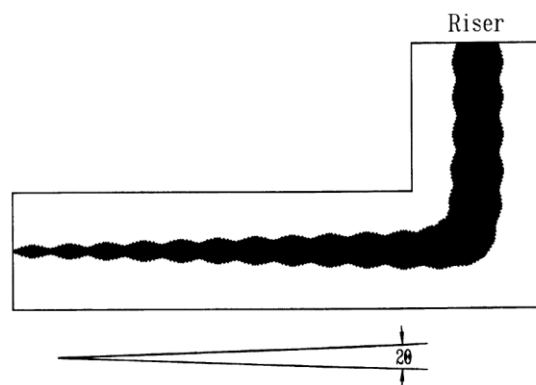


Figure 4: Schematic illustration of geometric model by Sigworth and Wang [45]

$$G_T^{cr} \geq \left(1 + \frac{2\Delta T_{SL} k_S t_C}{\rho_S \Delta H_f l^2} \right) \left(\frac{\rho_S \Delta H_f l}{4k_S t_C} \right) \tan\theta \quad [6]$$

Hansen and Sahn Model: Hansen and Sahn (1988) proposed another criterion which indicates that $G/V_S^{1/4} V_L^{1/2}$ (where V_L is flow velocity of liquid through the fixed dendrite skeleton and V_S is velocity of solid feeding] when less than a critical value will avoid porosity. They proposed this model considering the fact that velocity of flow in bar geometry is five to ten times more than that of plate geometry of the same thickness, resulting in additional feeding resistance experienced in bars compared to plates. But for both steel bars and plates, this critical value is $1 \text{ Ks}^{3/4} \text{ mm}^{-7/4}$ [37-41].

Limitation: This criterion is less used compared to Niyama criterion because of the need of flow velocities (V_S and V_L) whereas Niyama criterion requires only temperature distribution throughout the casting.

Dimensionless Niyama Criterion: Carlson and Beckermann (2008) proposed a Dimensionless Niyama Criterion (Ny^*) taking into consideration the local thermal conditions as well as the alloy material properties, solidification parameters and critical pressure required for pore formation.

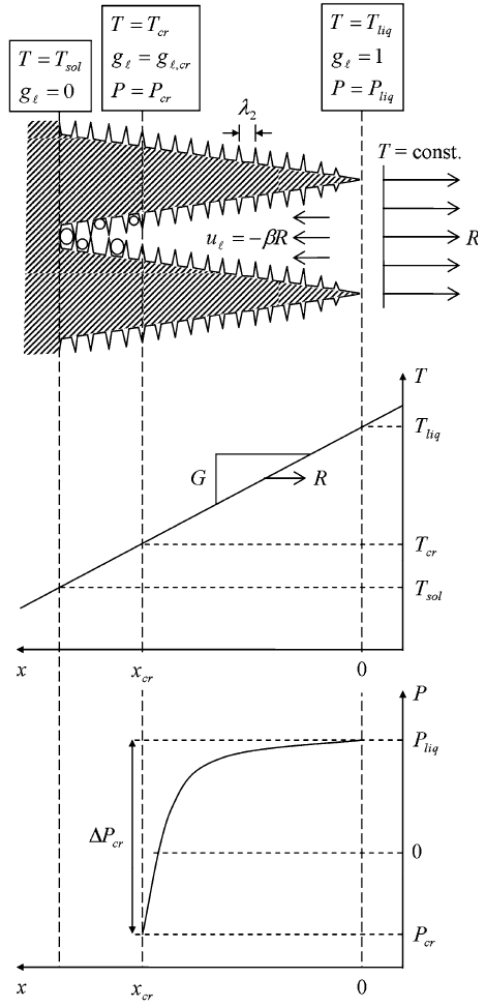


Figure 5: Schematic diagram of mushy zone solidifying with constant temperature gradient, G and isotherm velocity, R [42].

The solver uses the following equations to calculate Ny^* :

$$Ny^* = \frac{G\lambda_2\sqrt{\Delta P_{cr}}}{\sqrt{i\beta\Delta T_f\mu_l}} = Ny\frac{\lambda_2\sqrt{\Delta P_{cr}}}{\sqrt{\beta\Delta T_f\mu_l}} = \sqrt{I(g_{l,cr})} \quad [7]$$

where

$$I(g_{l,cr}) = \int_{g_{l,cr}}^1 180 \frac{(1-g_l)^2}{g_l^2} \frac{d\theta}{dg_l} dg_l \quad [8]$$

where G is thermal gradient, λ_2 is the secondary dendrite arm spacing (SDAS), ΔP_{cr} is critical pressure drop for stable pore to exist, \dot{T} is cooling rate, β is $(\rho_s - \rho_l)/\rho_l$, ΔT_f is the freezing range, μ_l is dynamic viscosity of liquid, Ny is Niyama criterion, $\theta = (T - T_{sol}) / \Delta T_f$ is a dimensionless number and g_l is liquid volume fraction.

The SDAS can be determined as a function of cooling rate from the relation:

$$\lambda_2 = C_\lambda \dot{T}^{-1/3} \quad [9]$$

Inserting equation [9] into equation [7] results in:

$$Ny^* = Ny C_\lambda \dot{T}^{-1/3} \sqrt{\frac{\Delta P_{cr}}{\beta \Delta T_f \mu_l}} \quad [10]$$

By assuming that local feeding flow ceases once shrinkage porosity forms, continuity equation can be simplified and integrated to give the following relation of final pore volume fraction (g_p)

$$g_p = \beta' g_{l,cr} \quad [11]$$

where $\beta' = \beta / (\beta + 1) = (\rho_s - \rho_l) / \rho_s$

Simulator uses the following sequence to determine final pore volume fraction (g_p):

$$Ny^* \rightarrow I(g_{l,cr}) \rightarrow g_{l,cr} \rightarrow g_p \quad [12]$$

Advantages:

- It is dimensionless and easy to handle
- Considers the local thermal conditions as well as the alloy material properties and solidification parameters
- Directly yields the pore volume fraction eliminating the need for estimation of a critical Niyama value
- Can be calculated by any simulation software in the same manner as the original Niyama criterion (Ny)
- Experimentally proven for steel, aluminum alloys, magnesium alloys and nickel based alloys [42, 43].

However, Sigworth contends that Niyama should not be used in first place to predict shrinkage because shrinkage formation is driven by freezing rate and gases in melt [44]. Carlson and Beckermann defended their work by replying that their model predicts shrinkage pores only and definitely not gas pores [45].

Limitation: It does not consider the complex nucleation and growth of pores phenomena.

Coupled with oxide distribution this criterion would work remarkably well.

Nucleation

Pore formation occurs by nucleation and growth phenomena. Fischer (1948) quantified the work required for a stable pore to exist.

$$\Delta G = \gamma A + P_e V - P_i V = 4\gamma\pi r^2 + \left(\frac{4}{3}\right)\pi r^3 (P_e - P_i) \quad [13]$$

where P_e is local pressure in liquid, V is volume of bubble, A is the area of liquid-gas interface and γ is interfacial energy per unit area, $(P_e - P_i)$ is the pressure difference between exterior and interior of bubble.

The critical radius r^* is:

$$r^* = 2\gamma / \Delta P^* \quad [14]$$

where radii smaller than r^* will disappear and not form a stable pore.

However, pressure required for nucleation is extremely high and almost impossible for pore to nucleate homogeneously (if melt is exceptionally clean). Atomic structure of liquid metals being close-packed random structures whereas for solid metals is close-packed regular structures causes strength of liquid metals are almost as high as those of solid metals : fracture strength of liquid iron corresponds to nearly 8 GPa. Non-metallic inclusions are potentially the weakest part of liquid metal (refer to Table II). Pore nucleation is more active in presence of non-metallic inclusions like oxides [5]. Casting defects associated with oxide films may present different morphology such as ‘tangled or network’, ‘layer oxide or globular oxide’ and ‘cloud or strip clustering particles’ [46-48]. Meidiani et al. (2012) developed 3-D phase field model to describe the complex morphology of pores growing in between solid phase [49].

Table II: Fracture Pressure for liquids [5]

Liquid	Surface Tension(N/m)	Atomic Diameter (nm)	ΔP^*		
			Hall Petch (atm)	From Fischer (atm)	Complex Inclusion (atm)
Water	0.072	-	-	1320	16
Mercury	0.5	0.3	16700	22300	200
Aluminum	0.9	0.29	31000	30000	360
Copper	1.3	0.26	50000	50000	600
Iron	1.9	0.25	76000	70000	850

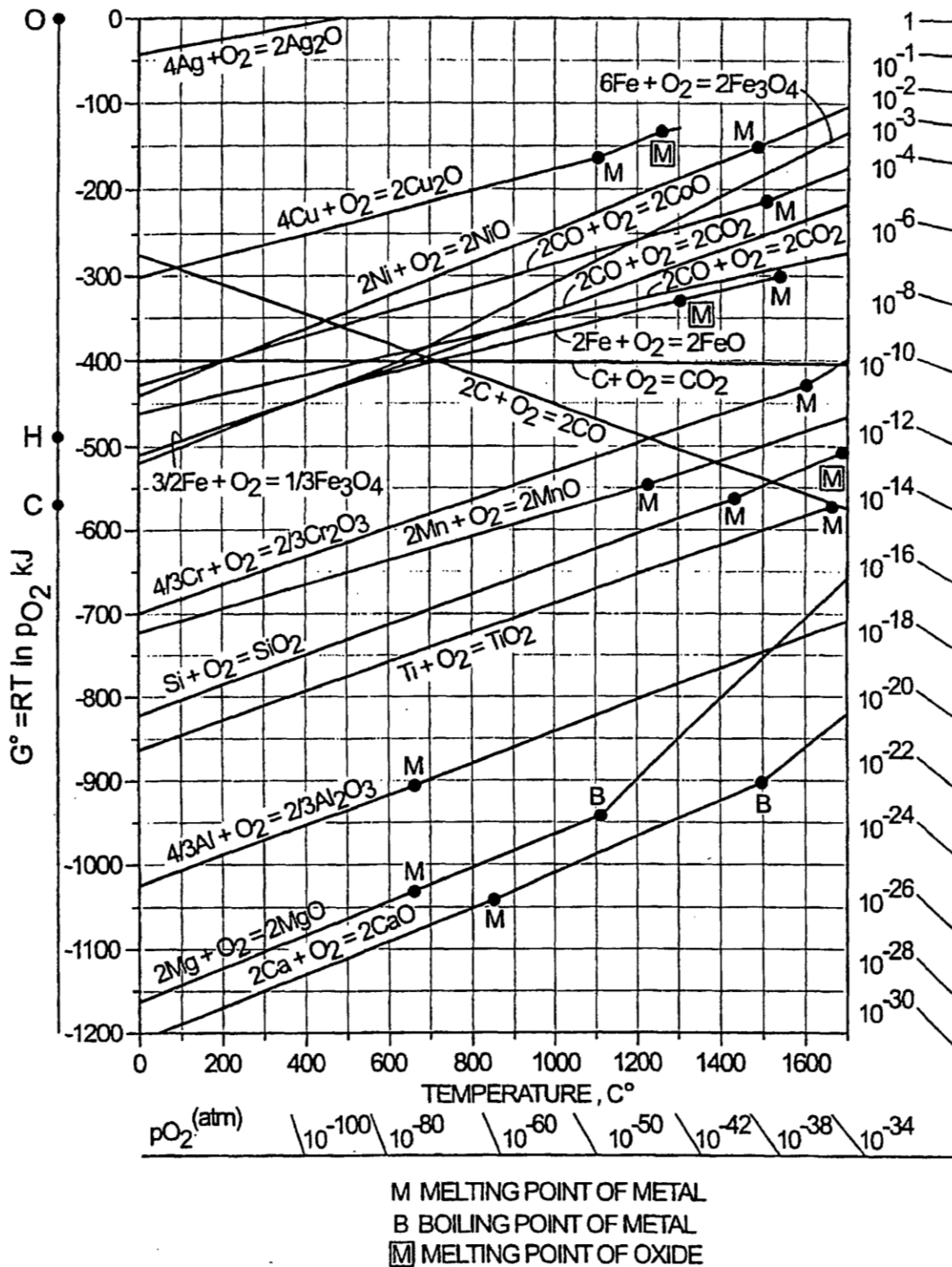
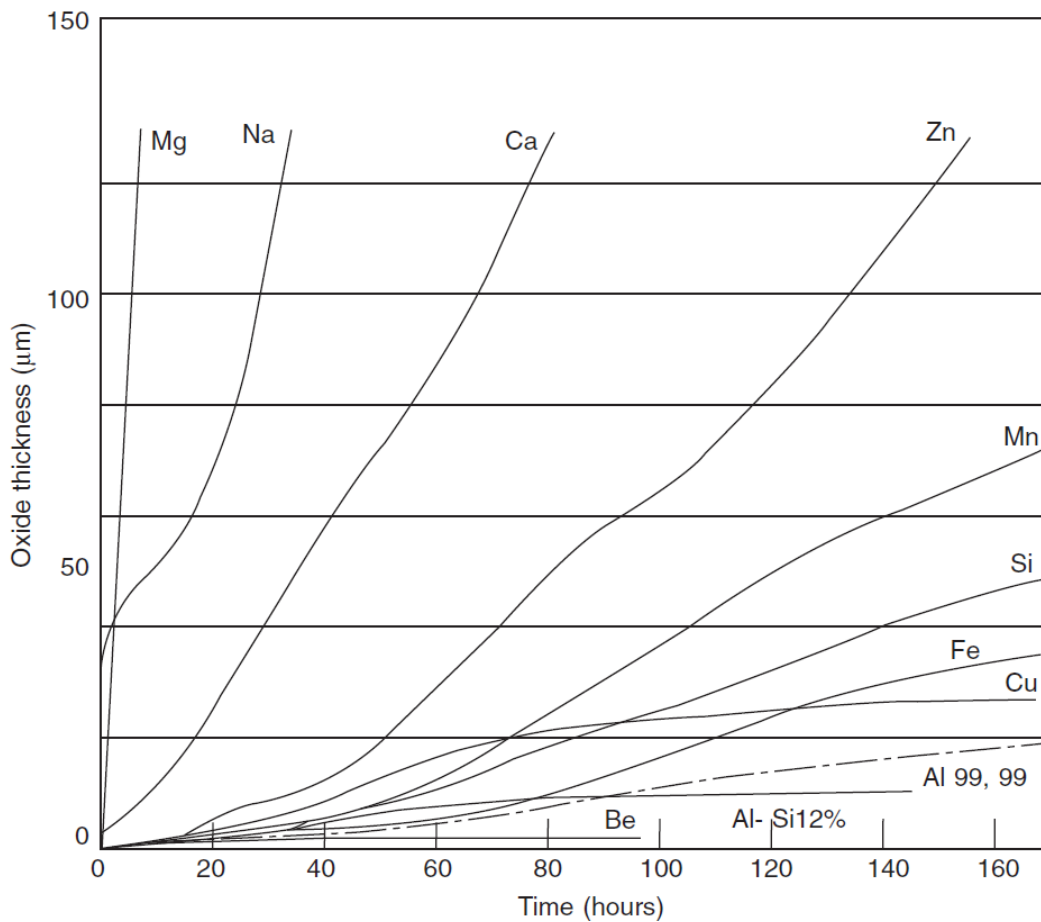
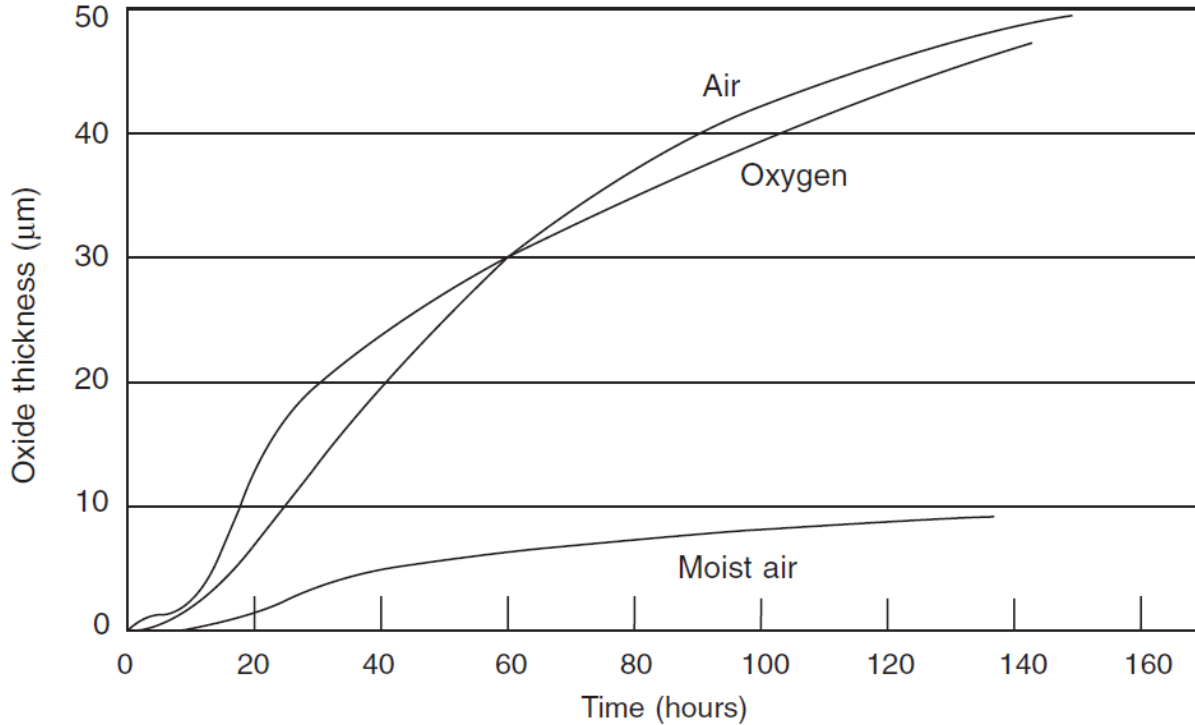


Figure 6: Ellingham Diagram referring to the tendency of aluminum to oxidize [68].

From a thermodynamic point of view, Figure 6 shows the tendency of aluminum to form oxides. Thiele studied the oxide growth on aluminum alloys with respect to time and also the oxidation in different environments: refer Figure 7 (a) and (b). Thiele experimentally found out the thickness of oxide film for liquid aluminum at 700°C to be 900 nm when melt was held for 1 hour. After 5 seconds at 700 °C the measured oxide film thickness was about 24 nm. When the oxide time was increased by a factor of ten, the oxide film thickness doubled [50].



(a)



(b)

Figure 7: (a) Effect of 1% of alloying element on aluminum at 800°C (b) Growth of pure aluminum in a flow of oxygen, dry and moist air [5, 50].

However, Campbell (1991) was the first to lend much insight into the oxidation behavior of a cast alloy. Oxides usually form a skin on the surface of liquid metal. Such oxide films can be entrained in bulk liquid. The oxide films for aluminum alloys may originate from two main sources: (a) “Old” oxide films formed during melt preparation (b) “Young” oxide films formed during the flow of metal in the gating system for a short time period [56]. These results are consistent with the study conducted by Runyoro et al. [51].

The entrainment action is the enfolding of surface leading to folding in and subduction of its surface film. These films being solid at the melt temperature, when get entrained, the dry

films fold facing each other cannot bond each other, being a ceramic- ceramic interface: see Figure 8.

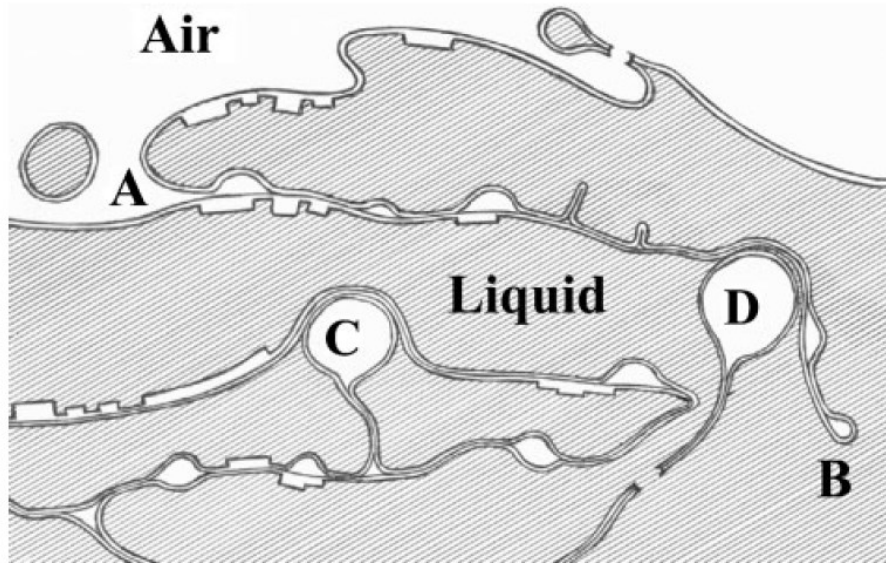


Figure 8: Formation of bifilm AB and bubbles CD creating bubble trails [5].

These bifilm cracks are usually invisible and often undetected because surface oxides are usually only a few molecules thick, approximately 20 nm.

Campbell (2003) derived a critical in-gate velocity of 0.5 m/s at which the surface will start to suffer from surface turbulence (breaking waves and entrainment of surface into the bulk) resulting into oxide bifilms causing random defects and reduced mechanical properties in castings [1, 5, 21, 26]. Surface turbulence is massive subject and studying the latter is out of the scope of this thesis.

2.5 Dimensionless Numbers

Weber Number: The concept of this critical velocity is enshrined in the Weber number, We . This dimensionless quantity is the ratio of inertial pressure in the melt ($\rho V^2/2$), with the pressure due to surface tension. This dimensionless quantity is the ratio of inertial pressure in the melt and pressure due to surface tension $\gamma/(1/r_1 + 1/r_2)$ where r_1 and r_2 are the radii of curvature of the surface in two perpendicular direction. If only curved in one plane the pressure becomes γ/r , or for a hemisphere where the orthogonal radii are equal, $2\gamma/r$ [5]. The use of Weber number does not enable tracking defects but it allows the quantification of entrainment. The criterion for entrainment is when critical Weber number ($We > 1$). In such conditions the inertial forces in the liquid that are tending to perturb the surface exceed the surface tension forces that tend to restrain the surface, holding it in a compact form [52, 53]. Critical Weber number correlates very well with critical in-gate velocity criterion, however according to Cuesta et al. (2006) surface entrainment is much more related to Weber number than to melt velocity [52, 54].

$$We = \rho L V^2 / \gamma \quad [15]$$

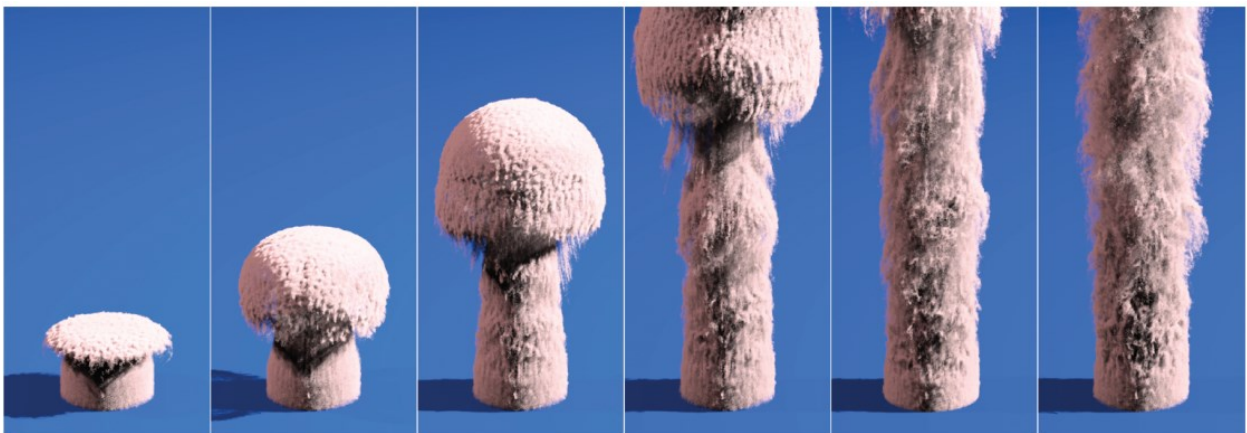


Figure 9: Smoke simulation showing the increase in amount of surface turbulence [55].

Froude Number: Froude number is the ratio of inertial pressure to gravitational pressure given as follows:

$$Fr = v / \sqrt{lg} \quad [16]$$

where v is velocity, g is gravitational acceleration, l is characteristic length. Isawa (1994) modeled water flow in a supposedly impermeable mold showing the vena contracta formation at the sprue and runner junction (a right angle turn of flow). The lesser is the life time of vena contracta, the better is the gating system due to decreased exposure to oxygen. Volume of air present in vena contracta and the Froude number of incoming flow were calculated and an empirical relationship was developed to calculate the time of flow of that Froude number to remove air in vena contracta [52, 56].

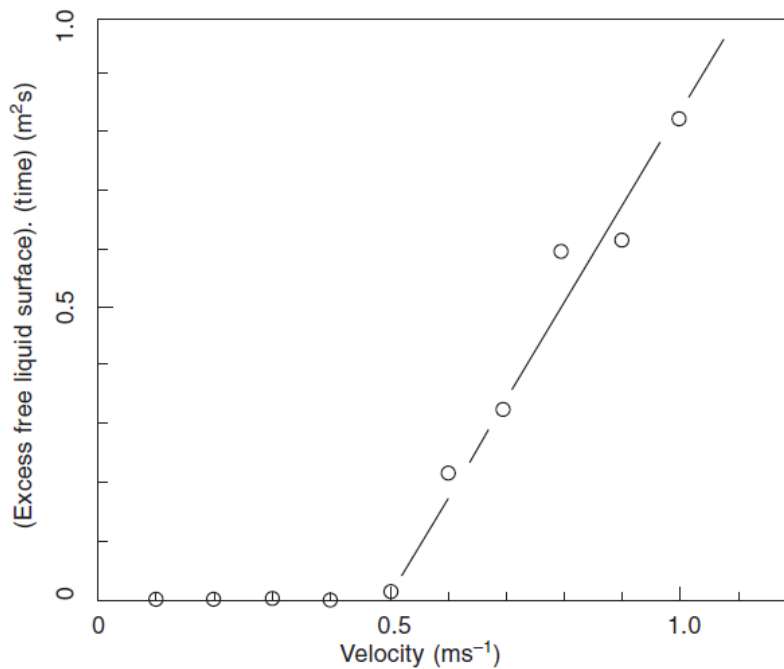


Figure 10: Computer simulation of excess free surface of melt as a function of gate velocity [1].

2.6 Review of Modeling of Oxide Films

Several attempts have been made to model the oxide entrainment during filling and melt treatment. Sako et al. (2001) and Ohnaka (2003) modeled micro-shrinkage formation based on entrapped oxide films [57, 58]. They assumed melt to be always covered with oxides and these oxide films are broken during collision of melt during mold filling, thereby being entrapped in the melt. Based on DFDM method [59] estimation of number and size of broken oxide films was calculated as follows:

$$N_{ox} = (\alpha_1 |u_{js1} - u_{js2}| + \alpha_2) S \quad [17]$$

$$S_{av} = \sum (S_M / N_{is}) \quad [18]$$

where N_{ox} is the number of entrapped oxides resulted from the collision, α_1 and α_2 are the parameters depending on alloy composition, S is the collision surface area, u_{js1} and u_{js2} are the velocity of the free surfaces, respectively, $|u_{js1} - u_{js2}|$ is the relative collision velocity, S_{av} is the average surface area of the broken oxides and S_M is the surface area of the broken oxide film. Oxide movement was tracked during fluid flow using:

$$l_v = u_v dt \quad [19]$$

where l_v is the distance of oxide movement (subscript v expresses the directions of x, y and z), u_v is the flow velocity of oxide which is set to the velocity of liquid flowing through the element and dt is the time step.

Campbell et.al (2006) has well summarized the current modeling methods in entrainment [56]. Carlson et al. (2009) modeled the oxide generation, growth and agglomeration of oxides and implemented in a general purpose simulation code [60]. Prakash et al. (2006) used meshless Smoothed Particle Hydrodynamics (SPH) method to oxide formation during mold filling stage in Direct Chill (DC) casting of extrusion billets [61-63]. In-depth description of SPH method is available [64-66]. Dai et al. (2012) developed an Oxide Film Entrainment Tracking Algorithm (OFET) method to simulate the movement of oxide films on the liquid metal surface [67].

3.0 DESCRIPTION OF NUMERICAL MODEL

3.1 Novaflow Model [76]

This model describes fluid flow in the mold. The Navier-Stokes equation is used:

$$\frac{\partial V_i}{\partial t} + V_j \frac{\partial}{\partial x_j} V_i = -\frac{1}{\rho} \frac{\partial P}{\partial x_i} + \frac{\partial}{\partial x_j} \nu \left(\frac{\partial V_j}{\partial x_i} + \frac{\partial V_i}{\partial x_j} \right) + g_i \quad [20]$$

$$\frac{\partial V_i}{\partial x_i} = 0 \quad [21]$$

where ρ is density, P is pressure, ν is kinematic viscosity and g_i is acceleration due to gravity.

Boundary conditions on the solid surface:

$$\left(\vec{v} \cdot \vec{n} \right) - \nu_n = 0 \quad [22]$$

where \vec{n} is the normal vector to the solid surface.

Calculation of pressure field, the following equation is solved:

$$\frac{\partial}{\partial x_i} \frac{1}{\rho} \frac{\partial P}{\partial x_i} = -\frac{\partial}{\partial x_i} \left(V_j \frac{\partial}{\partial x_j} V_i \right) + \frac{\partial}{\partial x_i} g_i \quad [23]$$

With boundary conditions:

- On free surface $P = 0$
- Taking into account equation [22] at solid surface

3.2 Novasolid Model [76]

This model describes heat flow in the casting. The volume fraction of solid phase $S(r, t)$, liquid phase $L(r, t)$ and empty phase $P(r, t)$ are related by the following equation:

$$S(r, t) + L(r, t) + P(r, t) = 1 \quad [24]$$

The phase balance in time derivations is follows:

$$\frac{\partial S(r, t)}{\partial t} + \frac{\partial L(r, t)}{\partial t} + \frac{\partial P(r, t)}{\partial t} = 0 \quad [25]$$

The law of conservation of mass is reduced to the following equation:

$$\rho_s(T) \frac{\partial S}{\partial t} + \frac{\partial}{\partial t} (\rho_L(T) L) = 0 \quad [26]$$

where $\rho_s(T)$ and $\rho_L(T)$ are temporal evolution of density of solid and liquid phases.

The mass conservation law for alloy species is reduced to following equation:

$$\rho_s(T)C_S^i(T)\frac{\partial S}{\partial t} + \frac{\partial}{\partial t}\left(C_L^i(T)\rho_L(T)L\right) = 0; \quad i = 1, 2, 3... \quad [27]$$

where $C_S^i(T)$, $C_L^i(T)$ are the concentrations of the i^{th} alloy component in the liquid and solid phases being in equilibrium at T temperature.

The basic equation being added to this system of equations: the equation of heat conduction with sources and convective heat transfer.

$$S\rho_s(T)Cp_s(T)\frac{\partial T}{\partial t} + L\rho_L(T)Cp_L(T)\left(\frac{\partial T}{\partial t} + V\nabla T\right) - q\rho_s(T)\frac{\partial S}{\partial t} = \text{div}(\lambda(T)\nabla T) \quad [28]$$

where $Cp_s(T)$, $Cp_L(T)$ are the specific heats of liquid and solids as a function of time at constant pressure, $\lambda(T)$ is the heat conduction coefficient of alloy with respect to time, q is the crystallization heat of alloy.

For the mold, the heat conduction equation is as follows:

$$\rho_K(T)Cp_K(T)\frac{\partial T}{\partial t} = \text{div}(\lambda_K(T)\nabla T) \quad [29]$$

where K indicates the similar properties for the mold.

If the convective heat transfer is neglected in equation [28] (e.g. small casting sizes), then equations [25 – 29] form closed system of four equations: $S(r, t)$, $L(r, t)$, $P(r, t)$, $T(r, t)$ which composes the heat flow model for NovaSolid.

3.3 Pore Nucleation Model

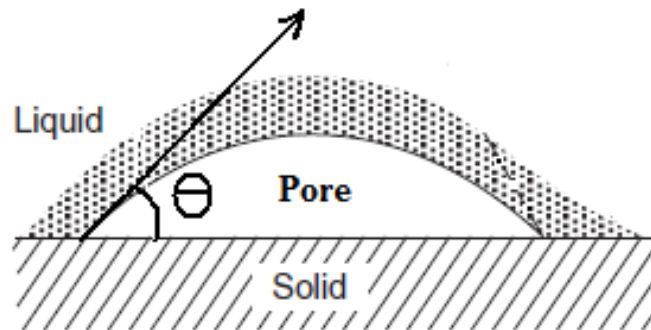


Figure 11: Geometry of a pore in contact with a solid surface.

Pores typically nucleate heterogeneously on non-wetted nuclei (when contact angle between solid and liquid exceeds 65°) [5]. Thus, oxides serve as good potential nucleation sites for pore formation [6-10, 70-72]. The criterion function developed in this study takes into account the nucleation potential for pore formation, which is crucial in accurately predicting the location and amount of pores in a casting.

A stochastic approach is adopted in this study to model the nucleation behavior of pores based on local oxide content. For both plate and bar geometries, oxide inclusions with different densities and sizes were introduced at different locations in the rigging system as well as the casting. Oxide particles were tracked after the solidification of the casting. Local oxide inclusion amount (n) was calculated as per simulation results shown in Fig. 18 and Fig. 25. The critical Niyama value was experimentally found to range from 0.3-0.5 for plate cast in furan mold at 20°C (see Fig. 20) [30].

It is assumed that pores will only grow when the following two conditions hold true simultaneously:

(i) $N_y < N_{y_{critic}}$ [30]

(ii) A randomly computer generated number, R_n ($0 \leq R_n \leq 1$) is smaller than the nucleation probability, P_n . The nucleation probability can be calculated as follows:

$$P_n = n / N \quad \text{where} \quad 0 \leq n \leq N \quad [31]$$

where N is the total oxide content, n is the predicted local oxide content that governs the nucleation of pores. This model was solved using Matlab code (Fig. 12).

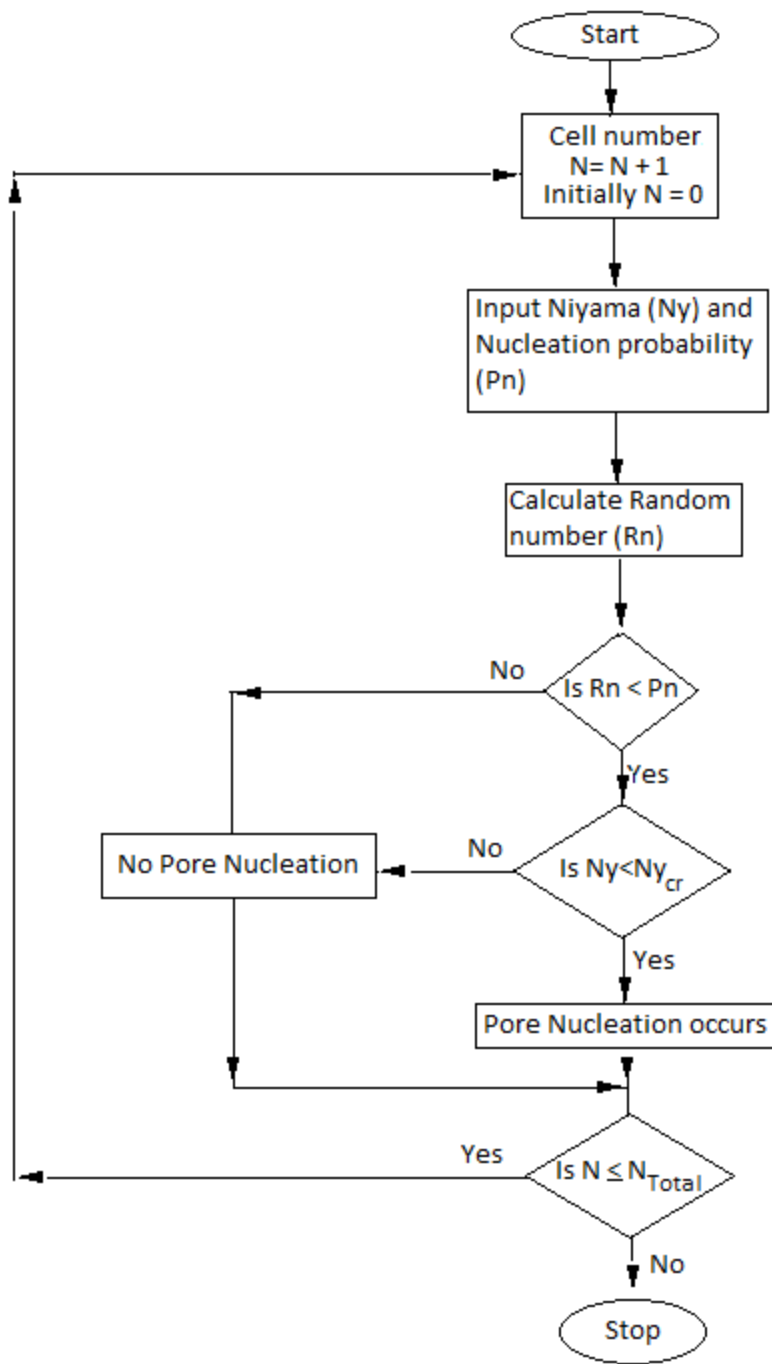


Figure 12: Flowchart for Matlab code

4.0 RESULTS AND DISCUSSION

4.1 Simulation Results

This model was tested on a cast A356 plate (500mm ×250mm×25mm) and A356 bar (250mm×20mm×20mm) using finite volume based NovaFlow&Solid simulation using the experimental data from [30] (Figs. 13-20).

The current nucleation model was solved using Matlab generating results as shown in Fig.22 and Fig. 26. This model matches reasonably well with the observed porosity defects shown in Fig. 21 and Fig. 27. This model does not consider oxide generation during filling and life-cycle of oxide bi-films. With the addition of these phenomena, the nucleation potential can be further refined to match results with pores formed after an actual metal pour. However, capturing the nucleation of pores requires a mesh size (of micron / millimeter scale) equivalent to the critical pore size to form a stable pore.

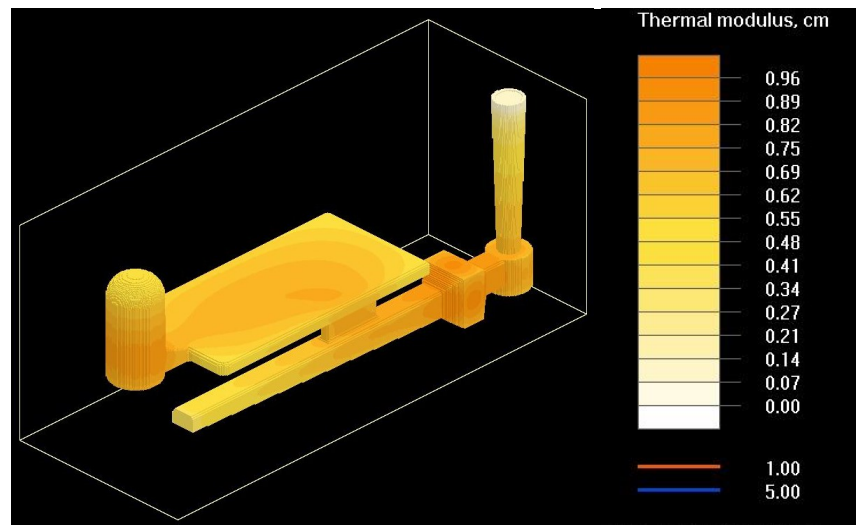


Figure 13: Modulus profile of for the 12.5 mm thickness cast A 356mm plate.

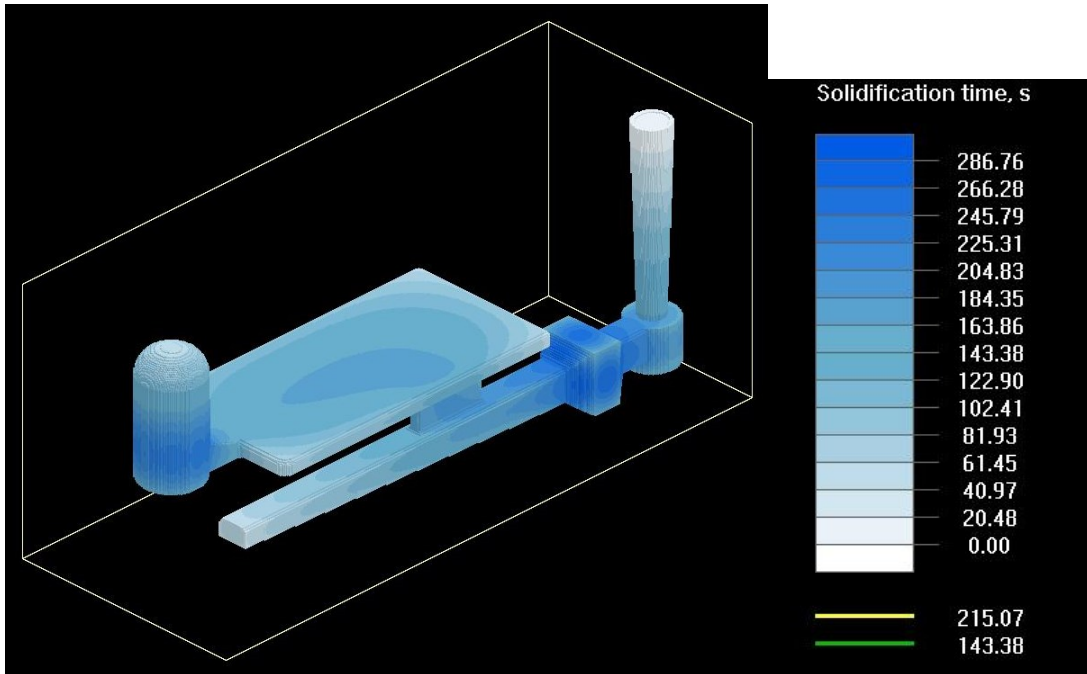


Figure 14: Solidification time profile for the 12.5 mm thickness cast A356 plate.

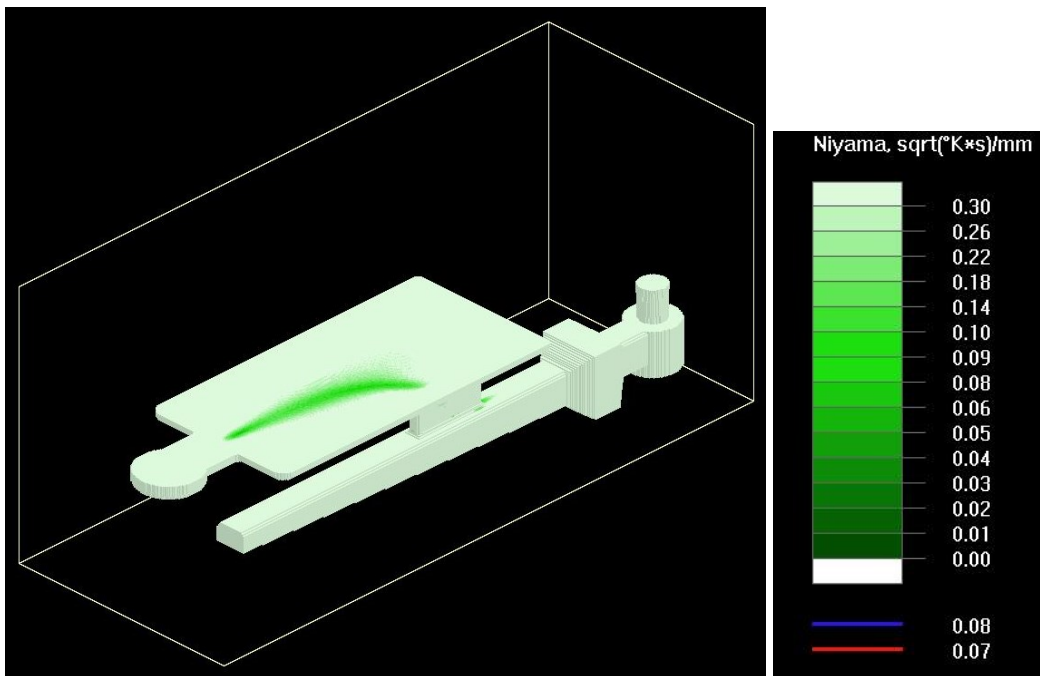


Figure 15: Profile for Niyama values for the cast A356 plate at 3% solid fraction.

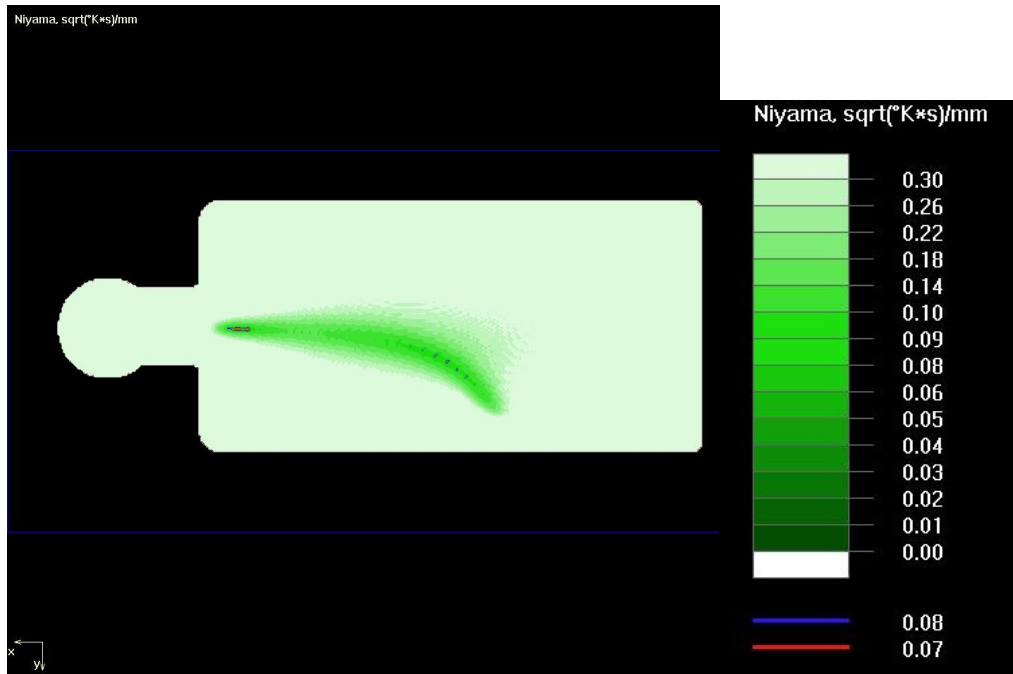


Figure 16: Niyama plot shown from the top view of the A356 plate at 3% solid fraction.

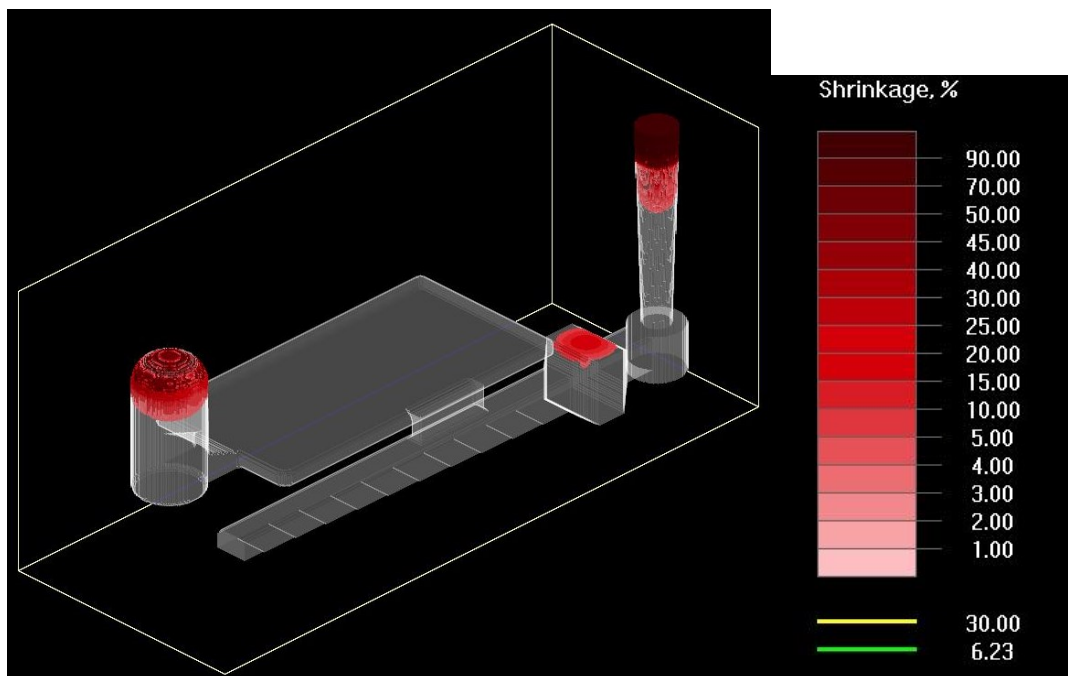


Figure 17: Shrinkage contraction plot in the cast the A356 plate.

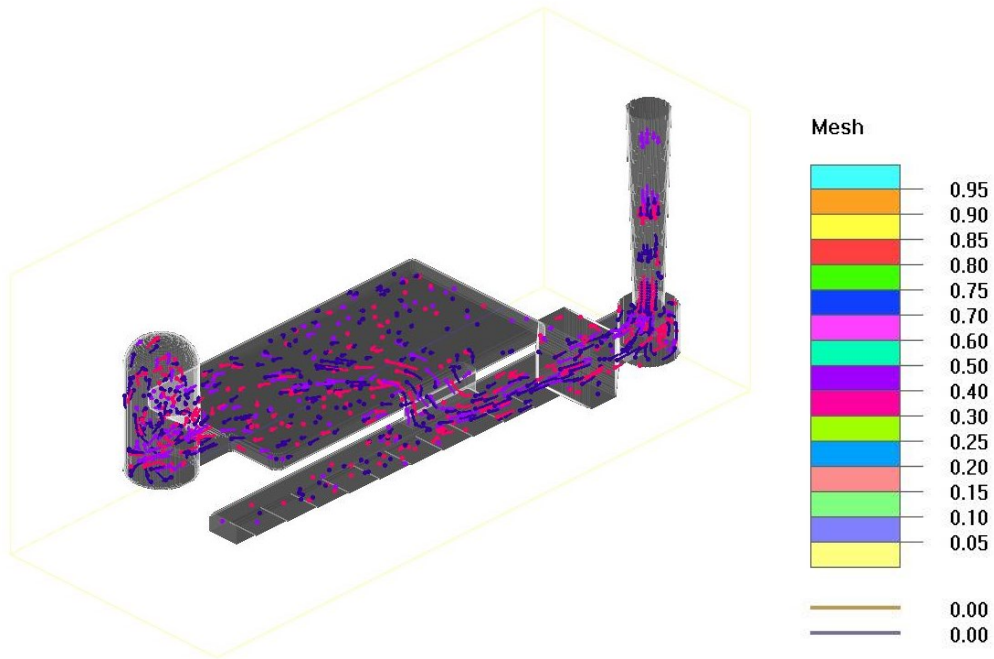


Figure 18: Distribution of oxides in the cast A356 plate.

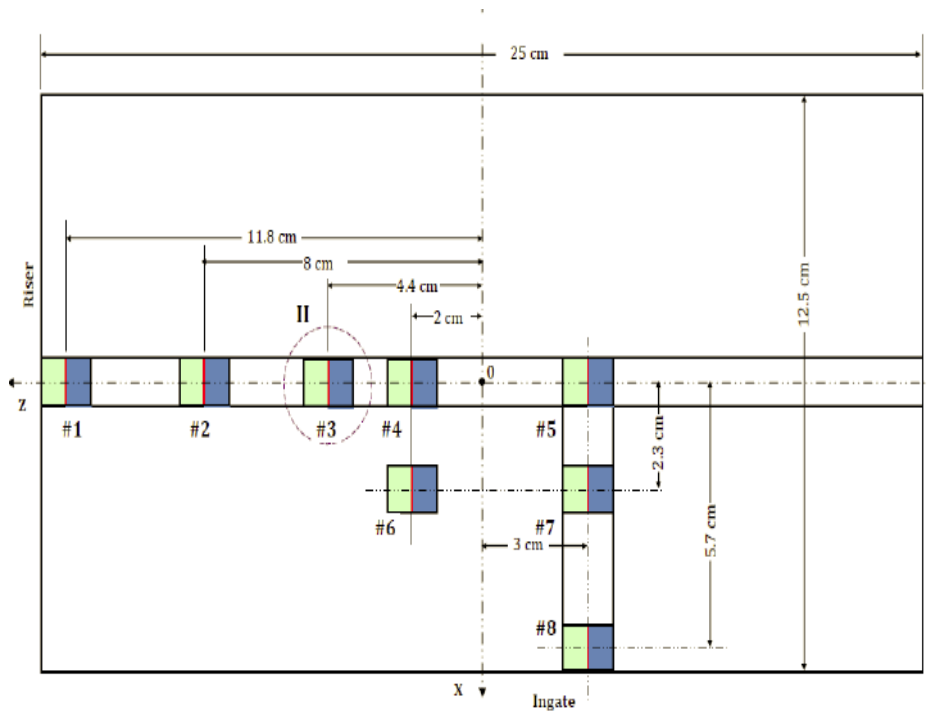


Figure 19: Measurement location for shrinkage prediction [30].

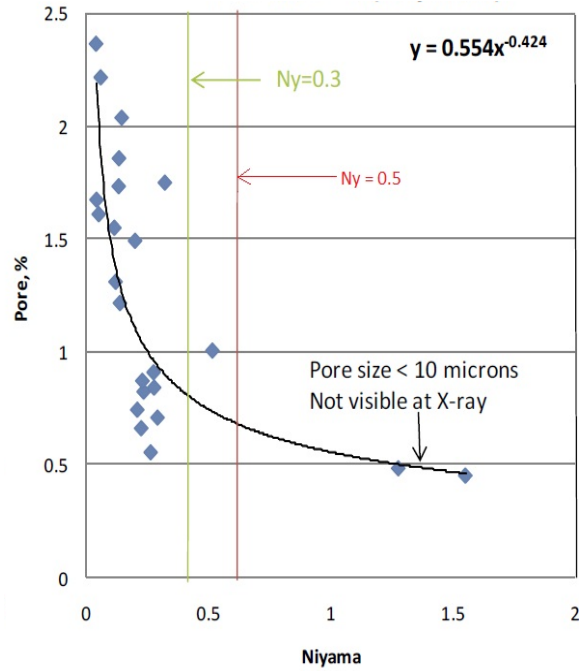


Figure 20: Niyama versus wt. % pore based on the measurements shown in Fig. 18 [30].

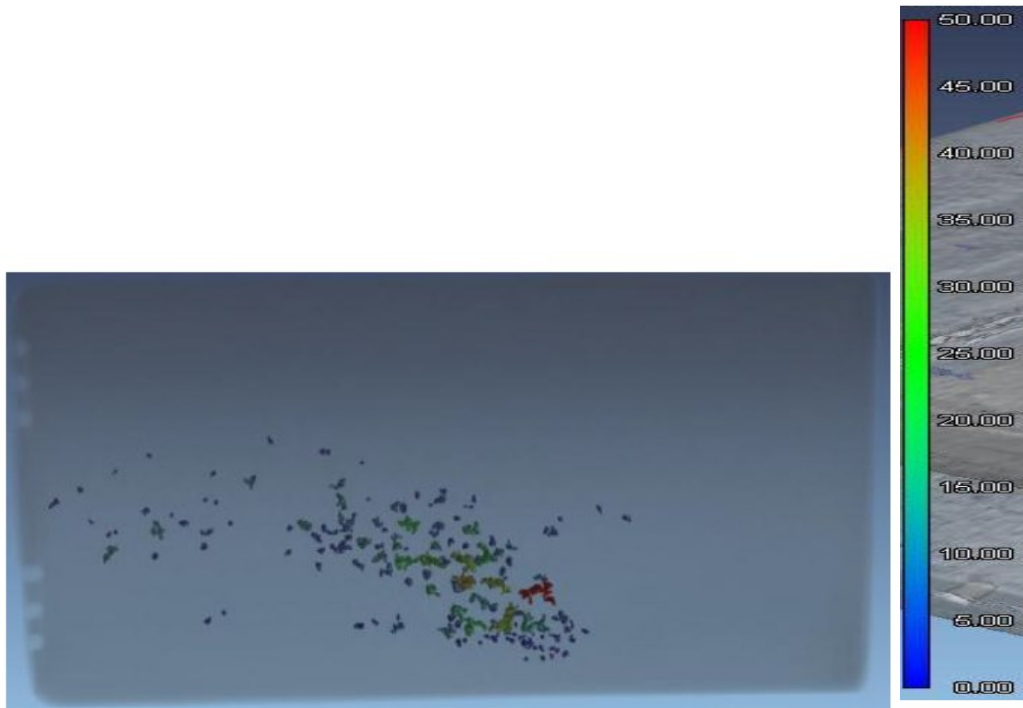


Figure 21: Computer tomography (CT) scan showing volume of gas/shrinkage defects/ mm^3 [30].

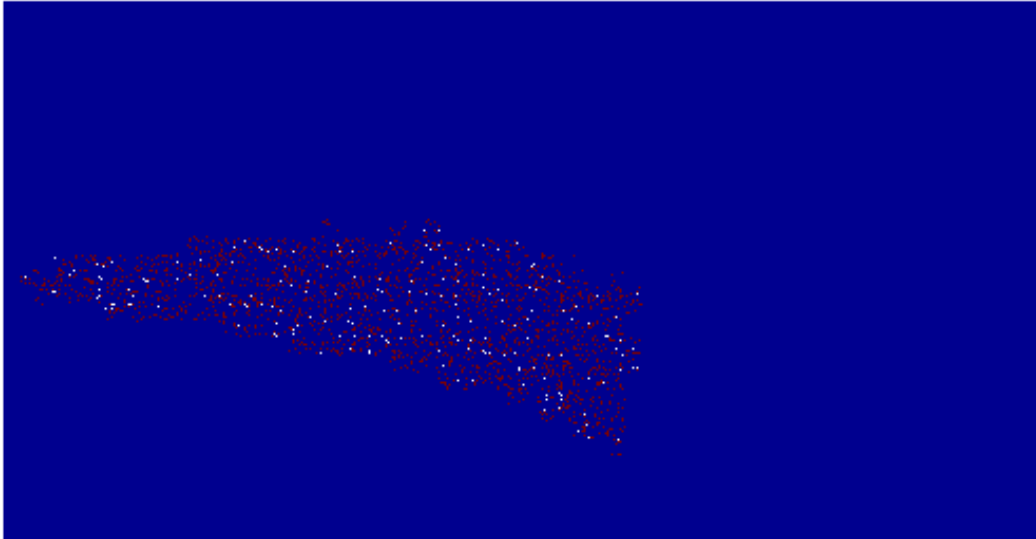


Figure 22: Stochastic behavior of pore nucleation obtained through MATLAB code.

Table III: Simulation Parameters

A356 (7 wt% Si, 0.35% Mg)	$T_L = 622\text{ }^{\circ}\text{C}$ $T_S = 571\text{ }^{\circ}\text{C}$
Melting Method	Resistive furnace / Induction Melting
Mold Media	Alphathane 1,2,3 binder
Pouring temperature (poured from furnace pout)	$710\text{ }^{\circ}\text{C}$
Pouring time	1.5 s
Solidification time	145 s

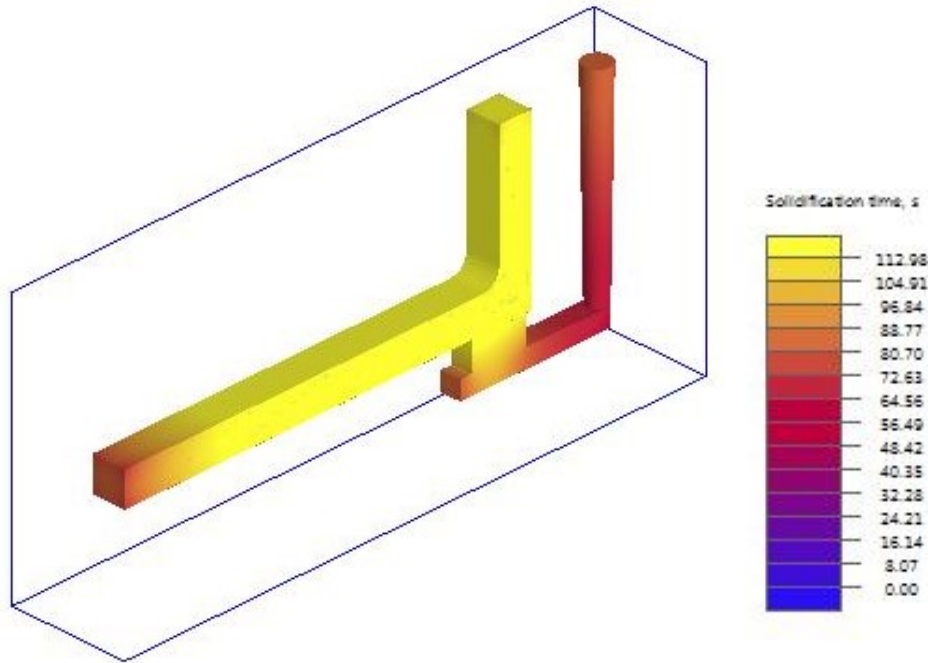


Figure 23: Solidification time plot in the 20 mm× 20 mm A356 bar geometry.

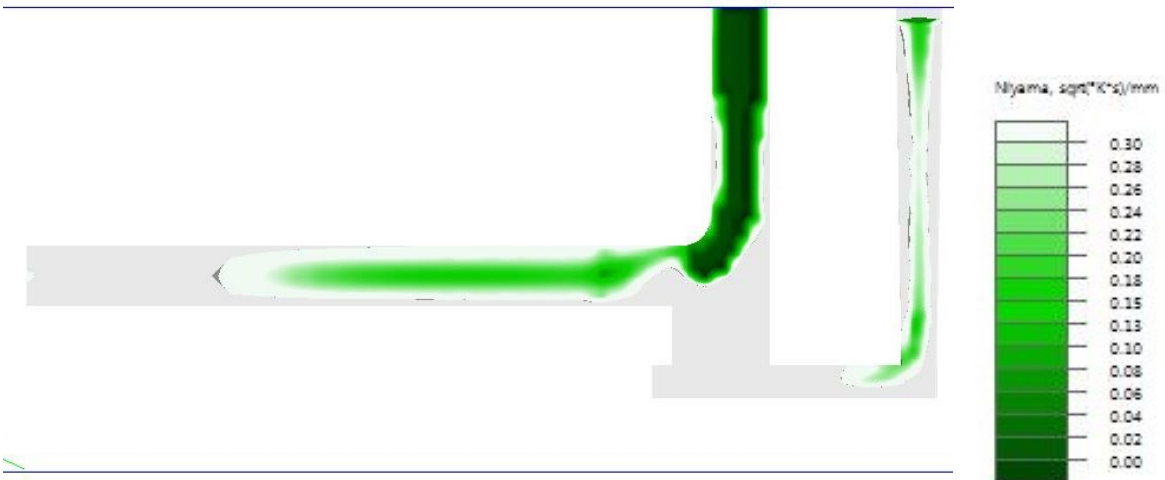


Figure 24: Niyama plot in the 20 mm× 20 mm A356 bar geometry at 3% solid fraction.

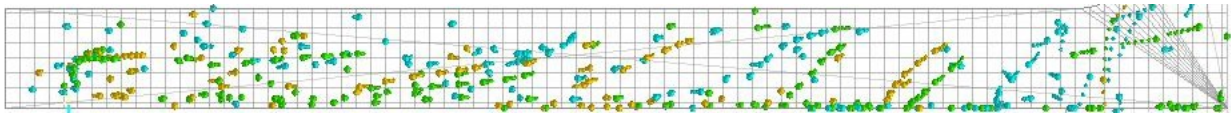


Figure 25: Distribution of oxides in a cast bar geometry after solidification.

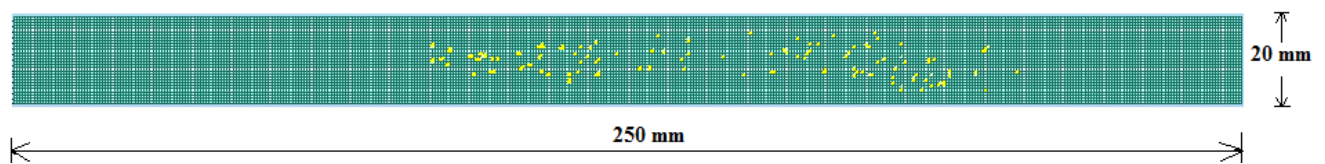


Figure 26: Stochastic behavior of pore nucleation obtained through MATLAB Code.

4.2 Experimental Results

The bar casting was poured using both: the resistive and the induction furnace with identical pouring conditions (except liquid metal surface was protected with argon gas for the induction furnace). The casting geometry was sectioned along the central line and polished. The unetched sample was observed under an optical microscope. Following the centerline, the sectioned bar was examined at an interval of 10 mm throughout the 250 mm plate. Total number of observations was 25. Areal pore fraction was determined [refer Fig. 26].

Observations for the sectioned bar processes via Induction Melting:

- Pore size was high enough to be visible to a naked eye.
- Pores were irregular in shape.

- On visual inspection they appeared to have dispersed uniformly throughout the bar.
- Induction melted A356 samples had much higher porosities compared to A356 processed via the resistive furnace. Repeating the revelation made by Berry (2006), the continuous circulation currents in the crucible containing the melt cause oxide films on the melt which get sucked inside and new melt surfaces are continuously generated for more oxide films to form [69].

Results for A356 bar processed via the Resistive Furnace:

- Pores were more prominent above the center line of the bar casting.
- Areal pore fraction was determined at intervals of 10 mm distance along the central line of bar [Fig. 27].
- The severity of pore formation was related to Niyama criterion [Fig. 28].
- Considering pores to be spherical, pore size was calculated at an interval of 10 mm and it was related to SDAS [Fig. 29].

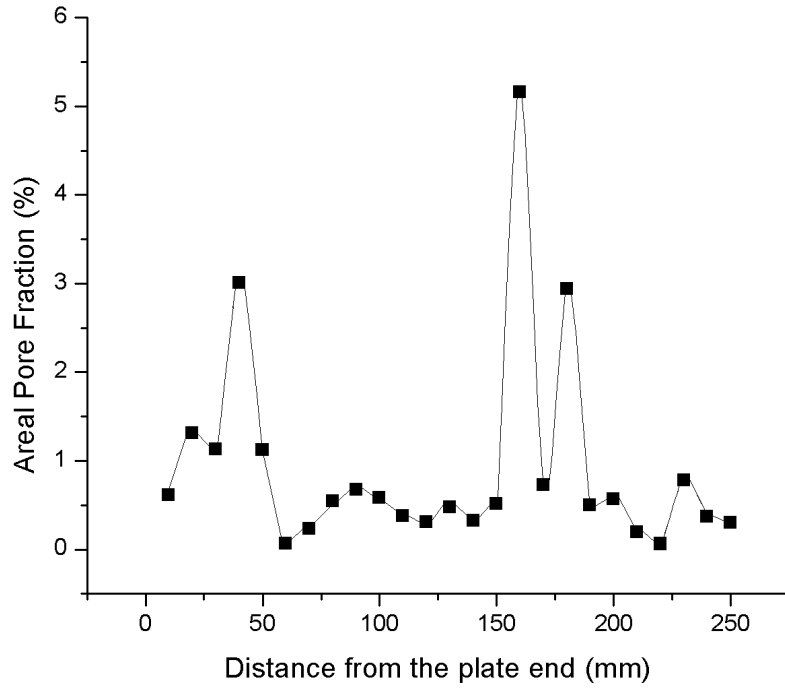


Figure 27: Areal pore % observed at different metallographic cross-sections of the bar.

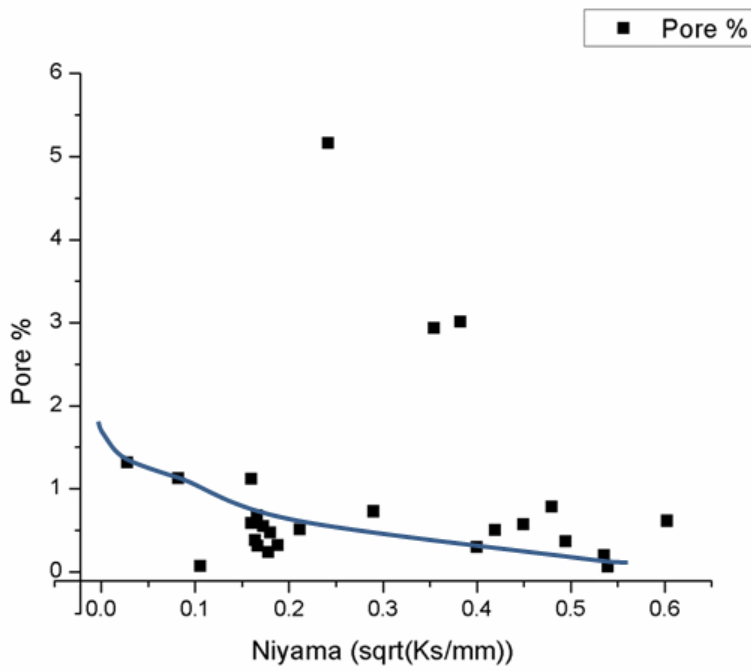


Figure 28: Effect of Niyama criterion on pore percentage.

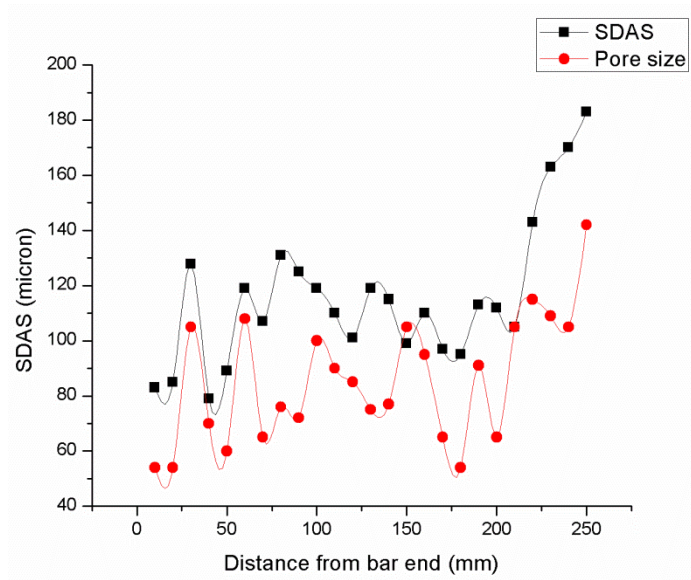
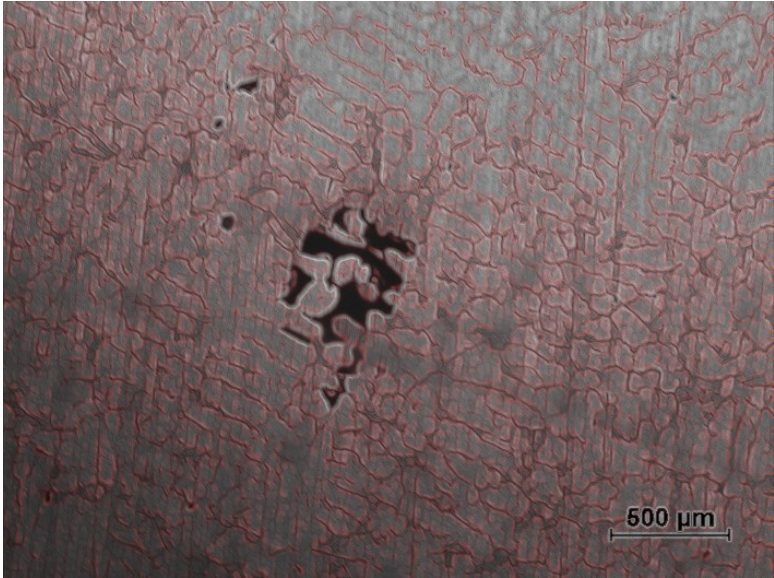
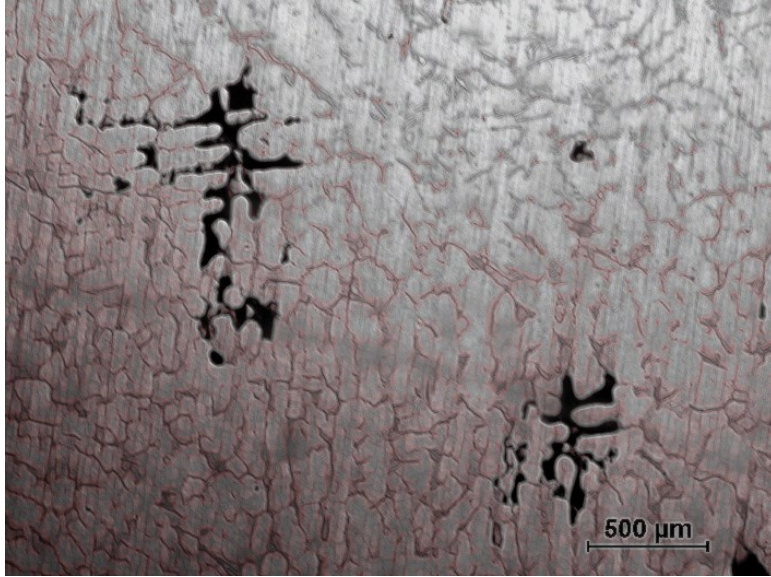


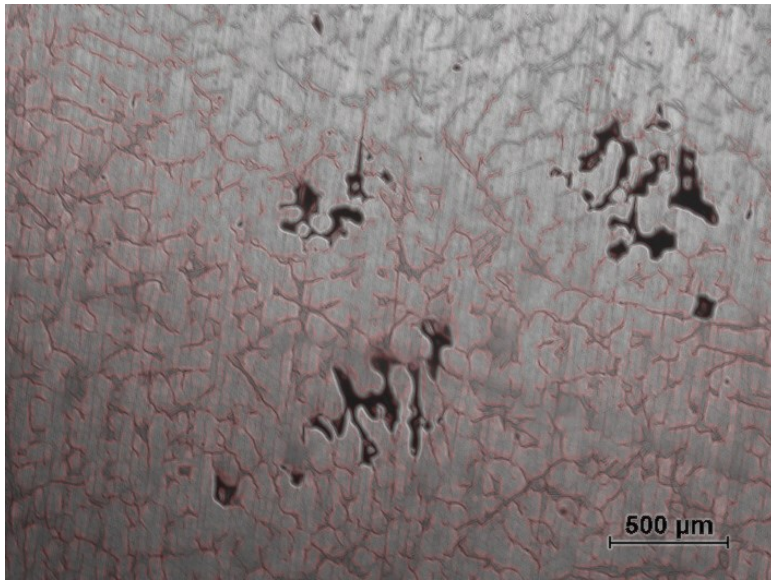
Figure 29: Comparing pore size with SDAS at an interval of 10 mm along the centerline of bar.



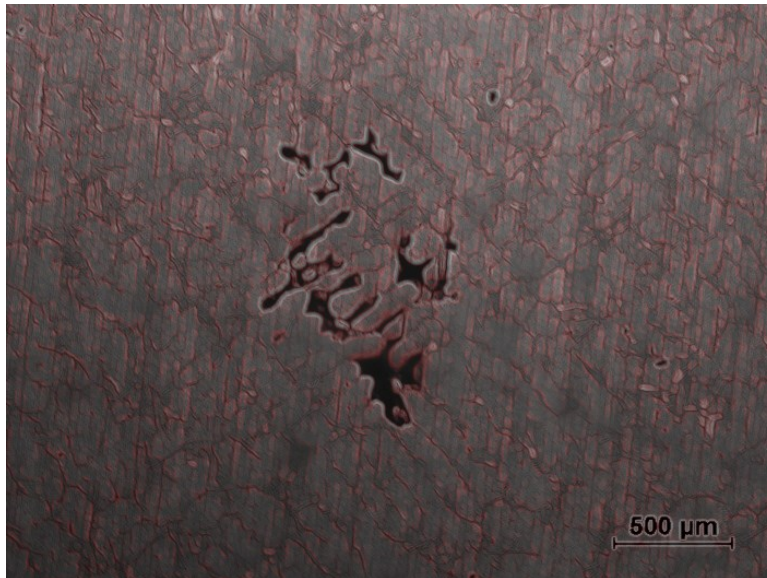
(a)



(b)



(c)



(d)



(e)

Figure 30: Typical examples of micro-shrinkage observed on metallographic cross-sections at: (a) 210 mm, (b) 230 mm, (c) 170 mm (d) 150 mm and (e) 140 mm from end of the plate.

5.0 CONCLUDING REMARKS AND FUTURE WORK

Conclusions:

- An attempt has been done to observe and model the stochastic behavior of nucleation of pores during casting solidification for A356 plate and bar.
 - The reoxidation effects of the liquid metal during mold filling and the oxide film entrapment may have a very strong effect on shrinkage porosity formation.
- Data for Niyama criterion values and oxide distribution were generated through NovaFlow&Solid simulation software and the model was solved using Matlab.
- The model for plate geometry matches reasonably to the experimentally measured pore defects in the A356 plate.
- However, following limitations need to be addressed:
 - This model does not include the pore growth model and hence cannot predict pore size.
 - The oxidation effects of the liquid metal during mold filling and the oxide film entrapment may have a very strong effect on shrinkage porosity formation.
 - The feasibility of this model also depends on the correct calculation of number, size and distribution of “old” oxide films and “young” oxide films formation which requires specification of melt treatment, melt handling, rigging system and other process specifications.
 - To capture the stochastic behavior of pore nucleation, the mesh size needs to be of the order of a few microns requiring high computational effort .

Future Work:

Future work will include:

- An improved model that will account for the phenomena discussed above
- Model validation for other cast alloys.
- Implement the developed micro-shrinkage model into the stochastic mesoscopic models for prediction of microstructure evolution of dendritic alloys [73-75]. This will improve significantly the predictions of the location and morphology (shape and size) of the micro-shrinkage that is forming in the interdendritic region or at the grain boundary.

REFERENCES

- [1] J. Campbell, Castings, 2nd edition , 2003, Butterworth-Heinemann, Oxford, UK.
- [2] J. Dantzig, M. Rappaz, Solidification, 1st edition, 2009 EFPL Press, Lausanne, Switzerland.
- [3] P.D. Lee, J.D. Hunt, “Hydrogen porosity in directionally solidified aluminum-copper alloys: A mathematical model”, Acta Materilia, vol. 49 (2001), pp. 1383-1398.
- [4] A. Catalina A. and C. Monroe, “A simplified model for quantitative shrinkage porosity prediction in steel castings”, IOP Conference Series: Materials Science and Engineering, vol. 33 (2012), pp. 12067-12074.
- [5] J. Campbell, Complete Casting Handbook: Metal Casting Processes, Techniques and Design 1st Edition, 2011 Elsevier, MA, USA.
- [6] D. Emadi, J. E. Gruzleski, M. Pekguleryuz, “Melt oxidation behavior and inclusion content in unmodified as Sr-modified A356 alloy- their role in pore nucleation”, AFS Transactions., vol. 104 (1996), pp. 763-768.
- [7] A. Kaye, A. Street, Die Casting Metallurgy, 1982, Butterworth, London, UK.
- [8] A. M. Samuel, F. H. Samuel, “Porosity factor in quality aluminum castings”, AFS Transactions, vol. 100 (1992), pp. 657-666.
- [9] C. J. Simenson, G. Berg, “A survey of inclusions in aluminum”, Aluminum, vol. 56 (1980), pp. 335-340.
- [10] P. S. Mohanty, F. H. Samuel, J. E. Gruzleski, “Experimental study on pore nucleation by inclusions in aluminum castings”, AFS Transactions, vol. 103 (1995), pp. 555-564.
- [11] X. Liu, “Ultrasonic cavitation-assisted molten metal processing of A356-Nanocomposites”, Master Thesis (2013), The University of Alabama.
- [12] D. Y. Ying, D. L. Zhang, “Processing of Cu-Al₂O₃ metal matrix nanocomposite materials by using high energy ball milling”, Materials Science and Engineering: A, vol. 286 (2000), pp. 152-156.
- [13] M. J. Kok, “Production and mechanical properties of Al₂O₃ particle-reinforced 2024 aluminum alloy composites”, Journal of Materials Processing Technology, vol. 161 (2005), pp. 381-387.

- [14] D. M. Stefanescu, ASM Handbook, Vol. 15: Casting, 1988, ASM International, Ohio, US.
- [15] J. Campbell, "Feeding Mechanisms in Castings", AFS Cast Metals Research Journal, Vol. 5 (1969), pp. 1-8.
- [16] A. K. Dahle, L. Arnberg, D. Apelian, "Burst feeding and its role in porosity formation during solidification of aluminum alloys", AFS Transactions, vol. 105 (1997), pp. 963-970.
- [17] A. K. Dahle, H. J. Thevik, L. Arnberg, D. H. StJohn, "Modeling the fluid-flow-induced stress and collapse in a dendritic network", Metallurgical and Materials Transactions B, vol. 30B (1999), pp. 287.
- [18] T. S. Piwonka, M.C. Flemings, "Pore formation in solidification", Transactions of the Metallurgical Society of AIME, vol. 236 (1966), pp.1157.
- [19] D. M. Stefanescu, Science and Engineering of Casting Solidification, 2nd Edition, 2008, Springer, N.Y., US
- [20] M. Tiryakioglu and J. Campbell, "Guidelines for designing metal casting research: application to aluminium alloy castings", International Journal of Cast Metals Research, vol. 20 (2007), pp. 25-29.
- [21] J. Berry, H. Huang, "Evaluation of criteria functions to minimize microporosity formation in long-freezing range alloys", American Foundry Society Transactions (1993), pp. 669-675.
- [22] J. Spittle, S. Brown, J. Sullivan, "Application of criteria functions to the prediction of microporosity levels in castings", Proceedings of the 4th Decennial International Conference of Solidification Processing, Sheffield (July 1997), pp. 251-255.
- [23] N. Chvorinov, "Theory of the solidification of castings", Giesserei, Vol. 27 (1940), pp. 177-186.
- [24] W.S. Pellini, "Factors which determine riser adequacy and feeding range, AFS Transactions, vol. 61 (1953), 61-80.
- [25] E. T. Myskowski, H. F. Bishop, W. S. Pellini, "Feeding range of joined sections", AFS Transactions, vol 61 (1953), pp. 302-308.
- [26] J. Campbell, Castings Practice: The Ten Rules of Castings, 1st edition, 2003, Butterworth-Heinemann, Oxford, UK.
- [27] P. N. Hansen, P. R. Sahm, "Modeling of casting, welding and advanced solidification processes IV", The Mineral, Metals and Materials Society (1988), Warrendale, PA, pp.33.
- [28] K. Kubo, R. D. Pehlke, "Mathematical modeling of porosity formation in solidification", Metallurgical and Materials Transactions, vol. 16B (1985), pp. 359-366.

- [29] E. Niyama E., T. Uchida, M. Morikawa. and S. Saito, “A method of shrinkage prediction and its application to steel castings practice”, AFS International Cast Metals Journal, vol. 7 (1982), pp. 52-63.
- [30] L. Nastac, “Modeling approach for quantitative prediction of macro-shrinkage and microshrinkage in A356 sand mould castings”, International Journal of Cast Metals Research, Vol 25, No. 3 (2012), 145-154.
- [31] K. D. Carlson, S. Ou, R. A. Hardin, C. Beckermann, “Development of new feeding distance rules using casting simulation: Part I: Methodology”, Metallurgical and Materials Transactions B, vol. 33B (2002), pp. 731-740.
- [32] K. D. Carlson, S. Ou, R. A. Hardin, C. Beckermann, “Development of a methodology to predict and prevent leakers caused by microporosity in steel castings”, Proceedings of the 55th SFSA Technical and Operating Conference, Chicago, IL, 2001.
- [33] K. D. Carlson, S. Ou, R. A. Hardin, C. Beckermann, “Feeding of High-Nickel alloy castings”, Metallurgical and Materials Transaction B, 2005, vol. 36B, pp. 843-856.
- [34] K. D. Carlson, Z. Lin, C. Beckermann, Metallurgical and Materials Transactions B, vol. 38B (2007), pp. 541-555.
- [35] S. Ou, K. D. Carlson, C. Beckermann, “Feeding and risering of high-alloy steel castings”, Metallurgical and Materials Transactions B, vol. 36B (2005), pp. 97-116.
- [36] G. K. Sigworth and C. Wang, “Evolution of porosity in long freezing range alloys”, Metallurgical and Materials Transactions B., vol. 24B (1993), pp. 365-377.
- [37] P. N. Hansen, P. R. Sahn, “How to model and simulate the feeding process in casting to predict shrinkage and porosity formation”, Modeling of Casting and Welding Process IV, TMS-AIME (1988), pp. 33-42.
- [38] P. N. Hansen, P. R. Sahn, “How to select and use criterion functions in solidification simulation”, AFS Transactions, vol. 101 (1993), pp. 443-446.
- [39] M. J. Jolly, H. S.Lo, M. Turan, J. Campbell, X. Yang, “Use of simulation rules in the practical development of a method for manufacture of cast iron camshafts”, Modeling of Casting, Welding and Advanced Solidification Processing IX, Aachen, Germany (2000).
- [40] H. Lo, J. Campbell, “The modeling of ceramic foam filters”, Modeling of Casting, Welding and Advanced Solidification Processes IX, Edited by P. N. Hansen, P. R. Sahn, 2000, pp. 373-380.
- [41] I. L. Svensson, A. Dioszegi, “Modeling of volume related defect formation in cast irons”, Modeling of Casting, Welding and Advanced Solidification Processes IX, Edited by P. Sahn, P. Hansen, Conley, 2000, pp. 102-109.

- [42] K. D. Carlson, C. Beckermann, "Prediction of Shrinkage Pore Volume Fraction using a Dimensionless Niyama Criterion", *Metallurgical and Materials Transactions A*, vol. 40A (2009), pp. 163-175.
- [43] K. D. Carlson, C. Beckermann, "Use of the Niyama Criterion to Predict Shrinkage-related Leaks in High-Nickel Steel and Nickel-Based Alloy Castings", *Proceedings of the 62nd SFSA Technical and Operating Conference*, Steel Founders' Society of America, Chicago, IL, 2008.
- [44] G. K. Sigworth, Discussion of "Prediction of Shrinkage Pore Volume Fraction using a Dimensionless Niyama Criterion", *Metallurgical and Materials Transactions A*, vol. 40A (2009), pp. 3051-3053.
- [45] K. D. Carlson, C. Beckermann, Reply: Author's reply to the Discussion of "Prediction of Shrinkage Pore Fraction using a Dimensionless Niyama Criterion", *Metallurgical and Materials Transactions A*, vol. 40A (2009), pp. 3054-3055.
- [46] M. Divandari, "Mechanism of bubble damage in casings", PhD Thesis, University of Birmingham, UK (2001), pp. 12-16.
- [47] N. R. Green, J. Campbell, "Influence in oxide film filling defects on strength of Al-7Si-Mg alloy castings", *AFS Transactions*, vol. 114 (1994), pp. 341-347.
- [48] W. Huang, J. W. Shu, S. T. Shih, "Diagnosis and analysis of oxide films in Al-Si-Mg alloys", *AFS Transactions*, vol. 108 (2000), pp. 547-560.
- [49] H. Meidani, J. Desbiolles, A. Jacot, M. Rappaz, "Three-dimensional phasefield simulation of micropore formation during solidification: Morphological analysis and pinching effect", *Acta Materialia*, vol.60 (2012), pp. 2518-2527.
- [50] W. Thiele, "The oxidation of melts of aluminum and aluminum alloys", *Aluminum*, Vol. 38 (1962), pp. 707-715 and 780-786.
- [51] J. Runyoro, S. Boutarabi, and J. Campbell, "Critical gate velocity for film forming casting alloys, a basis for process specification, *AFS Transactions*, vol. 100 (1992), pp. 225-234.
- [52] T. Isawa, "The control of the initial fall of liquid metal in gravity filled casting systems", Department of Metallurgy and Materials, The University of Birmingham, Birmingham, UK, 1994.
- [53] B. S. Massey, *Mechanics of Fluids*, 6th edition, 1992, Chapman & Hall, London, UK.
- [54] R. Cuesta, A. Delgado, A. Maroto, D. Mozo, "Numerically modeling oxide entrainment in the filling of castings: The effect of Weber number", *JOM*, vol. 58 (2006), pp. 62-65.
- [55] T. Kim, Nils Thürey, Doug James, and Markus Gross, "Wavelet turbulence for fluid simulation", *SIGGRAPH*, 2008.

- [56] J. Campbell, "The Modeling of entrainment defects during casting", TMS Annual Meeting, Simulation of Aluminum Shape Casting Processing: from Alloy Design to Mechanical Properties, TMS, San Antonio, TX, United States, 2006.
- [57] Y. Sako, I. Ohnaka, J.D. Zhu and H. Yasuda, "Modeling of oxide entrapment during mold filling of Al-alloy casting", Proceedings of the 7th Asian Foundry Congress, The Chinese Foundrymen's Association, Taipei (2001), pp. 363-369.
- [58] I. Ohnaka, Modeling of Casting, Welding and Advanced Solidification Processes X, eds. D.M Stefanescu et al., TMS, Warrendale Pa. 2003, pp. 403.
- [59] J. Zhu, I. Ohnaka, "Three Dimensional Computer Simulation of Mold Filling of Casting by Finite Difference Method", Transaction of Japan Foundrymen's Society, vol. 68 (1996), pp. 668-673.
- [60] K. D. Carlson, A. Melendez, C. Beckermann, "Modeling of Reoxidation inclusion in steel sand casting", Proceedings of the 63rd SFSA technical and Operating Conference, paper no. 5.6, Steel Founders Society, Chicago, IL, 2009.
- [61] M. Prakash, H. A. Joseph, P. Cleary, J. Grandfield, "Preliminary SPH modeling of oxide formation during the mold filling phase in DC casting of extrusion billets", Fifth International Conference on CFD in the Process Industries, CSIRO, Melbourne, Australia, 13-15 Dec., 2006.
- [62] P. W. Baker, K. Nguyen, R. Kirkaldie, "Dross generation of during transfer operations", 4th Australian Asian Pacific Conference, Aluminum Cast House Technology, TMS 1995, pp. 109-122.
- [63] J. Ha, P. W. Cleary, V. Alguine, T. Nguyen, "Simulation of die filling in gravity die casting using SPH and MAGMAsoft", Proceedings of 2nd International Conference on CFD in Minerals & Process Industries, 1999, Melbourne, Australia, pp. 423-428.
- [64] P. W. Cleary, J. Monaghan, "Conduction modeling using smoothed particle hydrodynamics", Journal of Computational Physics, vol. 148 (1999), pp. 227-264.
- [65] R. A. Gingold, J. Monaghan, "Smoothed particle hydrodynamics: Theory and application to non-spherical stars", Monthly Notices of Royal Astronomical Society, vol. 181 (1997), pp. 375-389.
- [66] J. Monaghan, "Smoothed particle hydrodynamics", Annual Review of Astronomy and Astrophysics, vol. 30 (1992), pp. 543-574.
- [67] X. Dai, M. Jolly, X. Yang, J. Campbell, "Modeling of liquid metal flow and oxide film defects of aluminum alloy castings", Materials Science and Engineering, vol. 33 (2012), pp. 1-10.

- [68] F. D. Richardson, *Physical Chemistry of Melts in Metallurgy*, Vol. 2 (1994), Academic Press, Massachusetts, US.
- [69] J. T. Berry, R. Luck, "Porosity criteria functions revisited", World Foundry Congress, Harrogate, UK, June 4-7, 2006.
- [70] S. Fox, J. Campbell, "Visualization of oxide film defects during solidification of aluminum alloys", *Scripta Materialia*, vol. 43 (2000), pp. 881-886.
- [71] C. Tian, J. Law, J van der Touw, M. Murray, J. Yao, D. Graham, D. John, "Effect of melt cleanliness on the formation of porosity defects in automotive aluminum high pressure die castings", *Journal of Materials Processing Technology*, vol. 122 (2002), pp. 82-93.
- [72] G. Backer, M. Ranganathan, J. Heimsch, M. McLaughlin, C. Kim, "Simulation of flow induced gas entrapment and its effect on porosity in aluminum die castings", *Conference of 2001 Die Casting in the 21st Century*, Cincinnati, October 29 – Nov. 1, 2001.
- [73] L. Nastac, *Modeling and Simulation of Microstructure Evolution in Solidifying Alloys*, Springer, 2004, Kluwer Academic Publishers, Boston, US.
- [74] L. Nastac, "Numerical Modeling of Solidification Morphologies and Segregation Patterns in Cast Dendritic Alloys", *Acta Materialia*, Vol. 47 (1999), No. 17, pp. 4253-4262.
- [75] L. Nastac, D. M. Stefanescu, "Stochastic Modeling of Microstructure Formation in Solidification Processes", *Modeling and Simulation in Materials Science and Engineering*, Institute of Physics Publishing, Vol. 5 (1997), No. 4, pp. 391-420.
- [76] NovFlow&Solid by Novacast: User Manual: <http://www.novacast.se/>